INTERNATIONAL JOURNAL OF COMPUTATIONAL FLUID DYNAMICS
https://doi.org/10.1080/10618562.2021.1991329

Taylor & Francis
Taylor & Francis Group



# A Gradient Compression-Based Compact High-Order Gas-Kinetic Scheme on 3D Hybrid Unstructured Meshes

Xing Ji[a], Wei Shyy[b] and Kun Xu[a,b,c]

[a]Department of Mathematics, Hong Kong University of Science and Technology, Kowloon, Hong Kong; [b]Department of Mechanical and Aerospace Engineering, Hong Kong University of Science and Technology, Kowloon, Hong Kong; [c]Shenzhen Research Institute, Hong Kong University of Science and Technology, Shenzhen, People's Republic of China

**ABSTRACT**

In this paper, a compact gas-kinetic scheme (CGKS) for compressible flow is constructed on hybrid unstructured mesh. Based on high-order gas evolution model at cell interfaces both cell-averaged flow variables and their gradients can be updated in CGKS and used in a compact third-order multi-resolution WENO reconstruction. In the precious CGKS, the flow variables at a cell interface are assumed to be continuous in space in the update of cell-averaged slopes. In order to improve the robustness of the scheme in discontinuous region in three-dimensional space, a compression factor for the cell-averaged gradients is proposed to take into account the possible discontinuity at cell interfaces. The accuracy of the scheme doesn't deteriorate with the implementation of the compression factor. Numerical tests from incompressible to hypersonic flow are presented to validate the high-order CGKS and demonstrate the effectiveness of the gradient compression factor for three-dimensional flow simulation on unstructured mesh.

**ARTICLE HISTORY**
Received 18 July 2021
Accepted 30 September 2021

**KEYWORDS**
Compact gas-kinetic scheme; multi-resolution WENO; gradient compression; Navier–Stokes solution; hybrid mesh

## 1. Introduction

The simulation of compressible flow with complex geometry is of vital importance in the engineering applications of aerospace industry. The use of unstructured mesh is especially favoured because of its geometric flexibility. The compact gas-kinetic scheme (CGKS) on tetrahedral mesh has been developed recently (Ji et al. 2021b). However, to resolve the viscous boundary layers efficiently, numerical methods based on the hexahedral or prismatic elements with high aspect ratio are preferred and they present more accurate and stable solutions than those methods on the tetrahedral elements alone. Therefore, the development of CGKS on hybrid mesh is necessary for real-world engineering applications.

Computational methods for compressible flow can be generally categorised into compact and non-compact methods in terms of the stencils used. As a non-compact scheme, the high-order finite volume methods (FVM) with the weighted essentially non-oscillatory (WENO) reconstruction have been developed and applied continuously in large-scale aeronautical simulations on hybrid unstructured mesh (Antoniadis, Tsoutsanis, and Drikakis 2017). The robustness of the schemes can be improved by the extended stencils used in reconstruction. However, they have difficulties in code portability, parallel programming, and boundary treatment.

On the other hand, methods with compact stencils have simple geometry dependency and bring great mesh adaptability and high scalability. The development of high-order compact methods becomes a hot topic nowadays. Two main representatives are the DG (Shu 2016) and the FR/CPR methods (Huynh 2007; Yu, Wang, and Liu 2014). By updating variables in multiple degrees of freedom (DOFs), these methods can achieve arbitrary spatial order of accuracy with only the targeted cell as the reconstruction stencil. Successful examples have been demonstrated in large eddy simulation (LES) (Z. J. Wang et al. 2017) and RANS simulation (Yang et al. 2019) for subsonic flows. For the flow simulation with discontinuities, these methods usually have less robustness against the traditional high-order FVMs. In addition, these methods have restricted explicit time steps and high memory consumption (Luo et al. 2010). The $P_NP_M$ (Dumbser

**CONTACT** Kun Xu makxu@ust.hk

2010) and reconstructed-DG (rDG) methods (Luo et al. 2010) target to overcome these weakness with the release of the compactness of the DG methods. In comparison with the DG methods, the same-order rDG methods can use larger time step and have less memory requirement.

In recent years, a class of high-order CGKS has been developed from the second-order gas-kinetic scheme (GKS) (Xu 2014). The CGKS is based on a time-accurate evolution model in the construction of the gas distribution function at a cell interface (Pan and Xu 2016). The time-dependent solution not only provides the fluxes across a cell interface but also gives the time-accurate flow variables. As a result, besides updating the cell-averaged conservative flow variables, the corresponding cell-averaged gradients can be updated simultaneously through the divergence theorem. The updating DOFs in CGKS are coming from the dynamic evolution solution rather than the weak formulation in the DG/rDG methods. Due to their differences, the CGKS can use a larger time step and has better robustness than the same-order DG methods. For example, a CFL number around 0.5 can be taken for the third-order CGKS (Ji et al. 2021a) while it is restricted to be less than 0.33 for the third-order P1P2-rDG scheme. The P1P2-rDG is claimed to be unstable on tetrahedral mesh with smooth reconstruction. However, the third-order CGKS is stable with a CFL number of 1 with the same compact stencil (Ji et al. 2021b). Another feature of GKS is to use the two-stage fourth-order temporal discretization method (Jiequan Li and Du 2016) or the so-called multi-stage multi-derivative time marching formulation (Seal, Güçlü, and Christlieb 2014). Although the gas-kinetic flux function is more expensive than the time-independent Riemann solvers, the GKS can achieve fourth-order temporal accuracy with only two stages (Pan et al. 2016), instead of four stages by the fourth-order Runge–Kutta (RK) time discretisation. Overall, the CGKS turns out to be more efficient in comparison with Riemann-solver-based RK methods (Ji et al. 2021a) in serial computation. Moreover, higher parallel efficiency is expected since less communication is required due to the less middle stages.

In this paper, the compact third-order GKS will be extended to mixed-element mesh. The scheme is linearly stable for smooth flow with unlimited constrained least-square reconstruction on a compact stencil involving von Neumann neighbours only. For discontinuous flow, the idea of the multi-resolution WENO reconstruction is adopted. The reconstruction is designed in a hierarchical way, i.e. the Nth-order of accuracy can be achieved by N central stencils from first-order to Nth-order (Zhu and Shu 2020). In previous work (Ji et al. 2021b), the smooth indicators are determined from the cell-averaged conservative flow variables and a two-step reconstruction is proposed to improve the robustness of the scheme. In the current work, the complexity of the spatial reconstruction is further reduced. Each low-order stencil is simply chosen as one cell in the compact stencil and the smooth indicator is directly obtained from the corresponding cell-averaged slopes. In this way, there is no extra memory requirement for the substencils and the computational cost for constructing the corresponding low-order polynomials is reduced. In case of discontinuous flow variables at a cell interface, the current gradient update scheme with continuous assumption of flow variables at cell interface will be revised in the updated gradients. In order to improve the mesh adaptability, the accuracy of updated solution, and the robustness of the scheme for flow simulation with strong shocks, a cell-averaged gradient compression factor (CF) will be proposed to modify the updated slope in the discontinuous flow region. Based on the CGKS framework, the CF is different from the existing priori or posteriori limiters (Krivodonova et al. 2004; Clain, Diot, and Loubère 2011; Xiangxiong Zhang 2017). It has the following features: (i) accuracy preserving; (ii) negligible computational cost; (iii) combined with the multi-resolution WENO reconstruction, the scheme can truly reduce to the first-order GKS once discontinuous solutions appear regardless of the local mesh quality. The resulting CGKS becomes efficient and robust, and easy to program. Stringent tests including hypersonic flow passing through a space vehicle validate the robustness of the current compact scheme with complex geometry.

This paper is organised as follows. The basic framework of the compact high-order GKS on unstructured mesh is presented in Section 2. In Section 3, the details for the spatial reconstruction on mesh with mixed elements are presented, including the construction of the CF. Numerical examples from nearly incompressible to hypersonic flows are given in Section 4. A concluding remark are given in the last section.

## 2. Compact Finite Volume Gas-Kinetic Scheme

The 3-D gas-kinetic BGK equation (Bhatnagar, Gross, and Krook 1954) is

$$f_t + \mathbf{u} \cdot \nabla f = \frac{g - f}{\tau}, \tag{1}$$

where $f = f(\mathbf{x}, t, \mathbf{u}, \xi)$ is the gas distribution function, which is a function of space $\mathbf{x}$, time $t$, particle velocity $\mathbf{u}$, and internal variable $\xi$. $g$ is the equilibrium state approached by $f$ and $\tau$ is the collision time.

The collision term satisfies the compatibility condition

$$\int \frac{g - f}{\tau} \boldsymbol{\psi} \, \mathrm{d}\Xi = 0,$$

where $\boldsymbol{\psi} = (1, \mathbf{u}, \frac{1}{2}(\mathbf{u}^2 + \xi^2))^T$, $\mathrm{d}\Xi = \mathrm{d}u_1 \, \mathrm{d}u_2 \, \mathrm{d}u_3 \, \mathrm{d}\xi_1 \cdots \mathrm{d}\xi_K$, $K$ is the number of internal degrees of freedom, i.e. $K = (5 - 3\gamma)/(\gamma - 1)$ in 3-D case, and $\gamma$ is the specific heat ratio.

In the continuum flow regime with the smoothness assumption, based on the Chapman–Enskog expansion the gas distribution function can be expressed as Xu (2014),

$$f = g - \tau D_{\mathbf{u}} g + \tau D_{\mathbf{u}}(\tau D_{\mathbf{u}}) g - \tau D_{\mathbf{u}}[\tau D_{\mathbf{u}}(\tau D_{\mathbf{u}}) g] + \cdots,$$

where $D_{\mathbf{u}} = \partial/\partial t + \mathbf{u} \cdot \nabla$. Different hydrodynamic equations can be derived by truncating on different orders of $\tau$. With the zeroth-order in truncated distribution function $f = g$, the Euler equations can be recovered by multiplying $\boldsymbol{\psi}$ on Equation (1) and integrating it over the phase space,

$$\mathbf{W}_t + \nabla \cdot \mathbf{F}(\mathbf{W}) = 0.$$

With the first-order truncation, i.e.

$$f = g - \tau(\mathbf{u} \cdot \nabla g + g_t),$$

the N-S equations can be obtained,

$$\mathbf{W}_t + \nabla \cdot \mathbf{F}(\mathbf{W}, \nabla \mathbf{W}) = 0,$$

with $\tau = \mu/p$ and $Pr = 1$.

The conservative flow variables and their fluxes are the moments of the gas distribution function

$$\mathbf{W}(\mathbf{x}, t) = \int \boldsymbol{\psi} f(\mathbf{x}, t, \mathbf{u}, \xi) \, \mathrm{d}\Xi, \tag{2}$$

and

$$\mathbf{F}(\mathbf{x}, t) = \int \mathbf{u}\boldsymbol{\psi} f(\mathbf{x}, t, \mathbf{u}, \xi) \, \mathrm{d}\Xi. \tag{3}$$

### 2.1. Compact Gas-Kinetic Scheme on Mixed-Elements

For a 3-D polyhedral cell $\Omega_i$, the boundary can be expressed as

$$\partial\Omega_i = \bigcup_{p=1}^{N_f} \Gamma_{ip},$$

where $N_f$ is the number of cell interfaces for cell $\Omega_i$. $N_f = 4$ for tetrahedron, $N_f = 5$ for prism and pyramid, $N_f = 6$ for hexahedron.

The semi-discretised form of FVM for conservation laws can be written as

$$\frac{\mathrm{d}\mathbf{W}_i}{\mathrm{d}t} = \mathcal{L}(\mathbf{W}_i) = -\frac{1}{|\Omega_i|} \sum_{p=1}^{N_f} \int_{\Gamma_{ip}} \mathbf{F}(\mathbf{W}(\mathbf{x}, t)) \cdot \mathbf{n}_p \, \mathrm{d}s, \tag{4}$$

with

$$\mathbf{F}(\mathbf{W}(\mathbf{x}, t)) \cdot \mathbf{n}_p = \int \boldsymbol{\psi} f(\mathbf{x}, t, \mathbf{u}, \xi) \mathbf{u} \cdot \mathbf{n}_p \, \mathrm{d}\Xi,$$

where $\mathbf{W}_i$ is the cell-averaged flow variables over cell $\Omega_i$, $|\Omega_i|$ is the volume of $\Omega_i$, $\mathbf{F}$ is the interface fluxes, and $\mathbf{n}_p = (n_1, n_2, n_3)^T$ is the unit vector representing the outer normal direction of $\Gamma_{ip}$. To evaluate the surface integral of fluxes, the iso-parametric transformation is used, which can be written as

$$\mathbf{X}(\xi, \eta) = \sum_{l=0}^{N_v} \mathbf{x}_l \phi_l(\xi, \eta),$$

where $\mathbf{x}_l$ is the location of the $m$th vertex for each element and $\phi_l$ is the base function (Qian Wang 2017). In this work, the linear element is considered, and a schematic for the transformation is shown in Figure 1.

After the transformation, the Gaussian quadrature points can be determined and $\mathbf{F}_{ip}(t)$ can be approximated by the numerical quadrature

$$\sum_{p=1}^{N_f} \int_{\Gamma_{ip}} \mathbf{F}(\mathbf{W}(\mathbf{x}, t)) \cdot \mathbf{n}_p \, \mathrm{d}s = \left|\Gamma_{ip}\right| \sum_{k=1}^{M} \omega_k \mathbf{F}(\mathbf{x}_{p,k}, t) \cdot \mathbf{n}_p, k.$$

To meet the requirement of a third-order spatial accuracy, three Gaussian points are used for a triangular face and four Gaussian points are used for a quadrilateral face. The details can be found in Pan and Xu (2020)

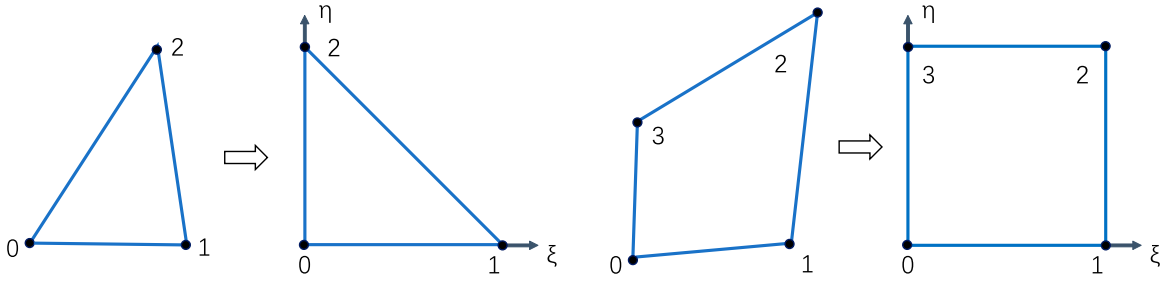


(a) Triangluar face (b) Quadrilateral face

**Figure 1.** The controlling points and iso-parametric transformation of the cell interfaces. (a) Triangluar face and (b) Quadrilateral face.

and Ji et al. (2021b). In the computation, the fluxes are obtained under the local coordinate. Details can be found in Ji et al. (2021b).

### 2.2. Gas-Kinetic Solver

Based on the integral solution of BGK equation (Xu 2014), a second-order time-accurate gas distribution function at a local Gaussian point $\mathbf{x} = (0, 0, 0)$ is constructed as

$$\begin{aligned} & f(\mathbf{0}, t, \mathbf{u}, \xi) \\ &= (1 - \mathrm{e}^{-t/\tau_n})g^c + [(t+\tau)\,\mathrm{e}^{-t/\tau_n} - \tau]a^c_{x_i}u_i g^c \\ &\quad + (t - \tau + \tau\,\mathrm{e}^{-t/\tau_n})A^c g^c \\ &\quad + \mathrm{e}^{-t/\tau_n} g^l[1 - (\tau + t)a^l_{x_i}u_i - \tau A^l]H(u_1) \\ &\quad + \mathrm{e}^{-t/\tau_n} g^r[1 - (\tau + t)a^r_{x_i}u_i - \tau A^r](1 - H(u_1)). \end{aligned} \tag{5}$$

The superscript $l$, $r$ represents the initial gas distribution function at the left and right sides of a cell interface with possible discontinuities. The superscript $c$ refers to evolved equilibrium state $g$ in space and time around a cell interface. The above solution basically states a physical evolution process from the particle free transport in the kinetic scale to the hydrodynamic flow evolution. The flow evolution at the cell interface depends on the ratio of time step to the local particle collision time $\Delta t/\tau$.

The initial $g^k$, $k = l, r$ has a form of a Maxwellian distribution

$$g^k = \rho^k \left(\frac{\lambda^k}{\pi}\right) \mathrm{e}^{-\lambda^k((u_i - U_i^k)^2 + \xi^2)},$$

which can be determined from the macroscopic variables $\mathbf{W}^l, \mathbf{W}^r$ through spatial reconstruction

$$\int \boldsymbol{\psi} g^l \,\mathrm{d}\Xi = \mathbf{W}^l, \int \boldsymbol{\psi} g^r \,\mathrm{d}\Xi = \mathbf{W}^r. \tag{6}$$

The spatial and temporal microscopic derivatives are denoted as

$$a_{x_i} \equiv (\partial g/\partial x_i)/g = g_{x_i}/g, \quad A \equiv (\partial g/\partial t)/g = g_t/g,$$

which is determined by the spatial derivatives of macroscopic flow variables and the compatibility condition as follows

$$\begin{aligned} \langle a_{x_1} \rangle &= \frac{\partial \mathbf{W}}{\partial x_1} = \mathbf{W}_{x_1}, \quad \langle a_{x_2} \rangle = \frac{\partial \mathbf{W}}{\partial x_2} = \mathbf{W}_{x_2}, \\ \langle a_{x_3} \rangle &= \frac{\partial \mathbf{W}}{\partial x_3} = \mathbf{W}_{x_3}, \\ \langle A + a_{x_1}u_1 + a_{x_2}u_2 + a_{x_3}u_3 \rangle &= 0, \end{aligned} \tag{7}$$

where $\langle \cdots \rangle$ are the moments of a gas distribution function defined by

$$\langle (\cdots) \rangle = \int \boldsymbol{\psi} (\cdots) g \,\mathrm{d}\Xi.$$

Similarly, the equilibrium state $g^c$ and its derivatives $a^c_{x_i}, A^c_{x_i}$ are determined by the corresponding $\mathbf{W}^c, \mathbf{W}^c_{x_i}$. The construction of the $\mathbf{W}^c, \mathbf{W}^c_{x_i}$ will be introduced in the next section. The details for the calculation of each microscopic term from macroscopic quantities can refer to Ji (2019).

For smooth flow, the time-dependent solution in Equation (5) can be simplified as Xu (2001)

$$f(\mathbf{0}, t, \mathbf{u}, \xi) = g^c - \tau(a^c_{x_i}u_i + A^c)g^c + A^c g^c t, \tag{8}$$

under the assumptions of $g^{l,r} = g^c$, $a^{l,r}_{x_i} = a^c_{x_i}$. The above gas-kinetic solver for smooth flow has less

numerical dissipations than the complete GKS solver in Equation (5).

In smooth flow region, the collision time is determined by

$$\tau = \mu/p,$$

where $\mu$ is the dynamic viscosity coefficient and $p$ is the pressure at the cell interface. In order to properly capture the un-resolved discontinuities, additional numerical dissipation is needed. The physical collision time $\tau$ in the exponential function part can be replaced by a numerical collision time $\tau_n$. For the inviscid flow, the collision time $\tau_n$ is modified as

$$\tau_n = \varepsilon\Delta t + C\left|\frac{p_l - p_r}{p_l + p_r}\right|\Delta t,$$

where $\varepsilon = 0.01$ and $C = 1$. For the viscous flow, the collision time is related to the viscosity coefficient,

$$\tau_n = \frac{\mu}{p} + C\left|\frac{p_l - p_r}{p_l + p_r}\right|\Delta t,$$

where $p_l$ and $p_r$ denote the pressure on the left and right sides of the cell interface.

### 2.3. Direct Evolution of the Cell-Averaged First-Order Spatial Derivatives

As shown in Equation (5), a time evolution solution at a cell interface is provided by the gas-kinetic solver, which is distinguished from the Riemann solvers with a constant solution. Recall Equation (2), the conservative variables at the Gaussian point $\mathbf{x}_{p,k}$ can be updated by taking the moments $\boldsymbol{\psi}$ on the gas distribution function,

$$\mathbf{W}_{p,k}(t^{n+1}) = \int \boldsymbol{\psi} f^n(\mathbf{x}_{p,k}, t^{n+1}, \mathbf{u}, \xi)\,\mathrm{d}\Xi, \quad k = 1, \ldots, M. \tag{9}$$

Then the cell-averaged first-order derivatives within each element at $t^{n+1}$ are given through the divergence theorem,

$$\begin{aligned}
\overline{W}_x^{n+1} &= \frac{1}{|\Omega|}\int_\Omega \nabla\cdot(\overline{W}(t^{n+1}), 0, 0)\,\mathrm{d}V \\
&= \frac{1}{|\Omega|}\int_{\partial\Omega}(1,0,0)\cdot\mathbf{n}\overline{W}(t^{n+1})\,\mathrm{d}S \\
&= \frac{1}{|\Omega|}\int_{\partial\Omega}\overline{W}(t^{n+1})n_1\,\mathrm{d}S \\
&= \frac{1}{|\Omega|}\sum_{p=1}^{N_f}\sum_{k=1}^{M_p}\omega_{p,k}W_{p,k}^{n+1}(n_1)_{p,k}\Delta S_p, \\
\overline{W}_y^{n+1} &= \frac{1}{|\Omega|}\int_\Omega \nabla\cdot(0, \overline{W}(t^{n+1}), 0)\,\mathrm{d}V \\
&= \frac{1}{|\Omega|}\int_{\partial\Omega}(0,1,0)\cdot\mathbf{n}\overline{W}(t^{n+1})\,\mathrm{d}S \\
&= \frac{1}{|\Omega|}\int_{\partial\Omega}\overline{W}(t^{n+1})n_2\,\mathrm{d}S \\
&= \frac{1}{|\Omega|}\sum_{p=1}^{N_f}\sum_{k=1}^{M_p}\omega_{p,k}W_{p,k}^{n+1}(n_2)_{p,k}\Delta S_p, \\
\overline{W}_z^{n+1} &= \frac{1}{|\Omega|}\int_\Omega \nabla\cdot(0, 0, \overline{W}(t^{n+1}))\,\mathrm{d}V \\
&= \frac{1}{|\Omega|}\int_{\partial\Omega}(0,0,1)\cdot\mathbf{n}\overline{W}(t^{n+1})\,\mathrm{d}S \\
&= \frac{1}{|\Omega|}\int_{\partial\Omega}\overline{W}(t^{n+1})n_3\,\mathrm{d}S \\
&= \frac{1}{|\Omega|}\sum_{p=1}^{N_f}\sum_{k=1}^{M_p}\omega_{p,k}W_{p,k}^{n+1}(n_3)_{p,k}\Delta S_p,
\end{aligned} \tag{10}$$

where $\mathbf{n}_{p,k} = ((n_1)_{p,k}, (n_2)_{p,k}, (n_3)_{p,k})$ is the outer unit normal direction at each Gaussian point $\mathbf{x}_{p,k}$.

### 2.4. Two-Stage Temporal Discretisation

The two-stage fourth-order (S2O4) temporal discretisation is adopted here as that in the previous CGKS (Zhao et al. 2020; Ji et al. 2021a). Following the definition of Equation (4), a fourth-order time-accurate solution for cell-averaged conservative flow variables $\mathbf{W}_i$ are updated by

$$\begin{aligned}
\mathbf{W}_i^* &= \mathbf{W}_i^n + \frac{1}{2}\Delta t\mathcal{L}(\mathbf{W}_i^n) + \frac{1}{8}\Delta t^2\frac{\partial}{\partial t}\mathcal{L}(\mathbf{W}_i^n), \\
\mathbf{W}_i^{n+1} &= \mathbf{W}_i^n + \Delta t\mathcal{L}(\mathbf{W}_i^n) \\
&\quad + \frac{1}{6}\Delta t^2\left(\frac{\partial}{\partial t}\mathcal{L}(\mathbf{W}_i^n) + 2\frac{\partial}{\partial t}\mathcal{L}(\mathbf{W}_i^*)\right),
\end{aligned} \tag{11}$$

where $\mathcal{L}(\mathbf{W}_i^n)$ and $\frac{\partial}{\partial t}\mathcal{L}(\mathbf{W}_i^n)$ are given by

$$\mathcal{L}(\mathbf{W}_i^n) = -\frac{1}{|\Omega_i|}\sum_{p=1}^{N_f}\sum_{k=1}^{M}\omega_{p,k}\mathbf{F}(\mathbf{x}_{p,k}, t_n)\cdot\mathbf{n}_{p,k}\Delta S_p,$$

$$\frac{\partial}{\partial t}\mathcal{L}(\mathbf{W}_i^n) = -\frac{1}{|\Omega_i|}\sum_{p=1}^{N_f}\sum_{k=1}^{M}\omega_{p,k}\partial_t\mathbf{F}(\mathbf{x}_{p,k},t_n)\cdot\mathbf{n}_{p,k}\Delta S_p,$$

$$\frac{\partial}{\partial t}\mathcal{L}(\mathbf{W}_i^*) = -\frac{1}{|\Omega_i|}\sum_{p=1}^{N_f}\sum_{k=1}^{M}\omega_{p,k}\partial_t\mathbf{F}(\mathbf{x}_{p,k},t_*)\cdot\mathbf{n}_{p,k}\Delta S_p.$$

The proof for the fourth-order accuracy in time is shown in Jiequan Li and Du (2016). The time-dependent gas distribution function at a cell interface is updated in a similar way,

$$f^* = f^n + \frac{1}{2}\Delta t f_t^n,$$
$$f^{n+1} = f^n + \Delta t f_t^*. \tag{12}$$

Thus, $f^*$ and $f^{n+1}$ are fully determined by Equation (5) or (8) and the macroscopic flow variables and their fluxes at the cell interface can be obtained simultaneously by Equations (2) and (3). The details can be found in Zhao et al. (2020). A fourth-order temporal accuracy for the Euler equations can be achieved for the conservative flow variables on arbitrary mesh by Equations (11) and (12). The complete proofs are given in Jiequan Li and Du (2016) and Zhao et al. (2020).

## 3. Compact Third-Order Reconstruction

In this section, the details for the construction of the compact reconstruction for smooth and discontinuous flows are presented. Especially, a special treatment, namely the cell-averaged slope compression factor, is introduced to improve the robustness of CGKS for supersonic and hypersonic flow simulation under irregular mesh.

### 3.1. Smooth Reconstruction

For a piecewise smooth function $Q(\mathbf{x})$ over cell $\Omega_0$, a polynomial $P^r(\mathbf{x})$ with degree $r$ can be constructed to approximate $Q(\mathbf{x})$ as follows

$$P^r(\mathbf{x}) = Q(\mathbf{x}) + O(\Delta h^{r+1}),$$

where $\Delta h \sim |\Omega_0|^{\frac{1}{3}}$ is the equivalent cell size. In order to achieve a third-order accuracy and satisfy conservative property, the following quadratic polynomial over cell $\Omega_0$ is needed

$$P^2(\mathbf{x}) = \overline{Q}_0 + \sum_{|k|=1}^{2} a_k p^k(\mathbf{x}),$$

where $\overline{Q}_0$ is the cell-averaged value of $Q(\mathbf{x})$ over cell $\Omega_0$, $k=(k_1,k_2,k_3)$, $|k| = k_1+k_2+k_3$. The $p^k(\mathbf{x})$ are basis functions, which are given by

$$p^k(\mathbf{x}) = x_1^{k_1}x_2^{k_2}x_3^{k_3} - \frac{1}{|\Omega_0|}\iiint_{\Omega_0} x_1^{k_1}x_2^{k_2}x_3^{k_3}\,\mathrm{d}V. \tag{13}$$

The volume integral in Equation (13) for a hexahedron $\Omega_0$ can be evaluated by the iso-parametric transformation described in Ji et al. (2021a). Other types of elements, i.e. tetrahedron, pyramid and prism, can be treated as the special cases of a hexahedron with some vertices merging together.

The quadratic polynomial $P^2(\mathbf{x})$ on $\Omega_0$ is constructed on the compact stencil $S_2$ including $\Omega_0$ and all its von Neumann neighbours, $\Omega_m, m=1,\ldots,N_f$, where the averages of $Q(\mathbf{x})$ and averaged derivatives of $Q(\mathbf{x})$ over each cell are known.

The following values on $S_2$ are used to obtain $P^2(\mathbf{x})$,

- cell averages $\overline{Q}$ for cell $0,\ldots,N_f$,
- cell averages of the $x$-direction partial derivative $\overline{Q}_{x_1}$ for cell $1,\ldots,N_f$;
- cell averages of the $y$-direction partial derivative $\overline{Q}_{x_2}$ for cell $1,\ldots,N_f$;
- cell averages of the $z$-direction partial derivative $\overline{Q}_{x_3}$ for cell $1,\ldots,N_f$.

The polynomial $P^2(\mathbf{x})$ is required to exactly satisfy

$$\iiint_{\Omega_m} P^2(\mathbf{x})\,\mathrm{d}V = \overline{Q}_m\,|\Omega_m|\,,$$

where $\overline{Q}_m$ is the cell-averaged value over $\Omega_m$, $m=1,\ldots,N_f$, with the following condition satisfied in a least-square sense

$$\iiint_{\Omega_m}\frac{\partial}{\partial x_1}P^2(\mathbf{x})\,\mathrm{d}V = (\overline{Q}_{x_1})_m|\Omega_m|,$$
$$\iiint_{\Omega_m}\frac{\partial}{\partial x_2}P^2(\mathbf{x})\,\mathrm{d}V = (\overline{Q}_{x_2})_m|\Omega_m|,$$
$$\iiint_{\Omega_m}\frac{\partial}{\partial x_3}P^2(\mathbf{x})\,\mathrm{d}V = (\overline{Q}_{x_3})_m|\Omega_m|,$$

where $\overline{Q}_{x_i}$, $i = 1, 2, 3$ are the cell-averaged directional derivatives over $\Omega_m$ in a global coordinate, respectively. The constrained least-square method is used to solve the above linear system (Wanai Li 2014). The left and right states $W^{l,r}$ provided by the reconstructed $P^2(\mathbf{x})$ yield a linearly stable third-order CGKS on hybrid mesh, as validated in Section 4.

### 3.2. Multi-Resolution WENO Procedure

In order to deal with discontinuity, the multi-resolution WENO reconstruction (Zhu and Shu 2020) is applied. Define three polynomials

$$\begin{aligned} p_2(\mathbf{x}) &= \frac{1}{\gamma_{2,2}} P^2(\mathbf{x}) - \sum_{\ell=0}^{1} \frac{\gamma_{\ell,2}}{\gamma_{2,2}} p_\ell(\mathbf{x}), \\ p_1(\mathbf{x}) &= \frac{1}{\gamma_{1,1}} P^1(\mathbf{x}) - \frac{\gamma_{0,1}}{\gamma_{1,1}} P^0(\mathbf{x}), \\ p_0(\mathbf{x}) &= P^0(\mathbf{x}). \end{aligned} \tag{14}$$

For a third-order reconstruction, the second-order polynomial $P^2(\mathbf{x})$ can be rewritten as

$$P^2(\mathbf{x}) = \gamma_{2,2} p_2 + \gamma_{1,2} p_1 + \gamma_{0,2} p_0, \tag{15}$$

with arbitrary positive coefficients $\gamma_{m,n}$ satisfying $\gamma_{0,2} + \gamma_{1,2} + \gamma_{2,2} = 1, \gamma_{0,1} + \gamma_{1,1} = 1$. The coefficients are chosen as $\gamma_{2,2} : \gamma_{1,2} : \gamma_{0,2} = 100 : 1 : 6$, and $\gamma_{1,1} : \gamma_{0,1} = 1 : 6$ as suggested in Zhu and Shu (2020).

The first-order polynomial $P^1(\mathbf{x})$ is determined solely from the targeted cell $\Omega_0$

- cell averages $\overline{Q}$ and cell averages of the $x_i$-direction partial derivatives $\overline{Q}_{x_i}$, i=1,2,3 for $\Omega_0$.

Thus, the $P^1(\mathbf{x})$ becomes

$$P^1(\mathbf{x}) = \overline{Q}_0 + \overline{Q}_{x_i} x_i, \quad i = 1, 2, 3.$$

The zeroth-order polynomial $P^0(\mathbf{x})$ is simply determined by the cell-averaged conservative variables on the targeted cell $\Omega_0$ itself, i.e. $P^0(\mathbf{x}) = \overline{Q}_0$.

The smoothness indicators $\beta_j$, $j = 1, 2$ are defined as

$$\beta_j = \sum_{|\alpha|=1}^{r_j} |\Omega|^{\frac{2}{3}|\alpha|-1} \iiint_\Omega \left(D^\alpha P_j(\mathbf{x})\right)^2 \mathrm{d}V, \tag{16}$$

where $\alpha$ is a multi-index and $D$ is the derivative operator, $r_1 = 1, r_2 = 2$. The smoothness indicators in Taylor series at $(x_0, y_0)$ have the order

$$\begin{aligned} \beta_2 &= O\{|\Omega_0|^{\frac{2}{3}}[1 + O(|\Omega_0|^{\frac{2}{3}})]\} = O(|\Omega_0|)^{\frac{2}{3}} = O(h^2), \\ \beta_1 &= O\{|\Omega_0|^{\frac{2}{3}}[1 + O(|\Omega_0|^{\frac{1}{3}})]\} = O(|\Omega_0|)^{\frac{2}{3}} = O(h^2). \end{aligned}$$

Assuming a suitable $\beta_0$

$$\beta_0 = O\{|\Omega_0|^{\frac{2}{3}}[1 + O(|\Omega_0|^{\frac{1}{3}})]\} = O(|\Omega_0|)^{\frac{2}{3}} = O(h^2),$$

a global smoothness indicator $\sigma$ similar to that in Zhu and Shu (2020) can be defined

$$\begin{aligned} \sigma^{3rd} &= \left(\frac{1}{2}(|\beta_2 - \beta_1| + |\beta_2 - \beta_0|)\right)^{\frac{4}{3}} \\ &= O(|\Omega_0|^{\frac{4}{3}}) = O(h^4). \end{aligned}$$

Then, the corresponding non-linear weights are given by

$$\begin{aligned} \omega_{m,n} &= \gamma_{m,n}\left(1 + \frac{\sigma}{\epsilon + \beta_m}\right), \\ \bar{\omega}_{m,n} &= \frac{\omega_{m,n}}{\sum \omega_{m,n}} = \gamma_{m,n} + O(h^2), \end{aligned} \tag{17}$$

where $m = 0, 1, 2$ when $n = 2$; $m = 0, 1$ when $n = 1$, and $\epsilon$ takes $10^{-16}$ to avoid zero in the denominator.

Replacing $\gamma_{m,n}$ by the normalised non-linear weights $\bar{\omega}_{m,n}$ in Equation (15), the final reconstructed polynomials are given by

$$R^{3rd}(\mathbf{x}) = \bar{\omega}_{2,2} p_2 + \bar{\omega}_{1,2} p_1 + \bar{\omega}_{0,2} p_0. \tag{18}$$

As a result, the non-linear reconstruction meets the requirement for a third-order accuracy $R(\mathbf{x}) = P(\mathbf{x}) + O(h^3)$. If any of these values yields negative density or pressure, the first-order reconstruction is used instead. The desired non-equilibrium states at Gaussian points can be obtained from the weighted polynomials

$$Q^{l,r}_{p,k} = R^{l,r}(\mathbf{x}_{p,k}), \quad (Q^{l,r}_{x_i})_{p,k} = \frac{\partial R^{l,r}}{\partial x_i}(\mathbf{x}_{p,k}).$$

In order to improve the robustness of the compact scheme, a two-step reconstruction has been designed and the smooth indicator of the zeroth-order polynomial $P^0(\mathbf{x})$ as a non-linear combination of the first-order biased sub-stencil on tetrahedron mesh (Ji et al. 2021b). In this paper, however, these sub-stencils are simply chosen as each neighbouring cell

- cell averages $\overline{Q}_j$ and cell averages of the $x_i$-direction partial derivatives $\overline{Q}_{x_i,j}$, $i = 1, 2, 3$ for cell $j = 1, \ldots, N_f$.

The smooth indicators for each stencils are

$$\begin{aligned}\beta_{0,j} &= |\Omega_0|^{\frac{2}{3}}(b_{1,j}^2 + b_{2,j}^2 + b_{3,j}^2)\\ &= |\Omega_0|^{\frac{2}{3}}(\overline{Q}_{x_1,j}^2 + \overline{Q}_{x_2,j}^2 + \overline{Q}_{x_3,j}^2).\end{aligned}$$

In this way, the sub-stencils are only single-cell involved. Thus, the smooth indicators are less affected by the local bad geometry. In addition, the WENO procedure becomes more simple and less memory-consuming. For the current reconstruction, only the coefficients for $P^2(\mathbf{x})$ are stored. Specially, a coefficient matrix with dimension $9 \times M$ is needed, where $M = 16$ for tetrahedron, $M = 24$ for hexahedron. The detailed formulation for the smooth indicator $\beta_0$ is given as

$$\begin{aligned}\sigma^{1st} &= \left[\frac{1}{\frac{1}{2}N_f(N_f-1)}\left(\sum|\beta_{0,j}-\beta_{0,k}|\right)\right]^{\frac{4}{3}},\\ \omega_j^{1st} &= 1 + \frac{\sigma^{1st}}{\epsilon+\beta_j},\\ \bar{\omega}_j^{1st} &= \frac{\omega_j}{\sum\omega_j},\\ \beta_0 &= \min\left(\sum\bar{\omega}_j^{1st}\beta_{0,j}, \beta_{0,0}\right),\end{aligned}$$

where $j, k = 1, \ldots, N_f$ and $j > k$.

However, such a choice is not robust enough for high-speed flow. To improve the robustness of the spatial reconstruction for the CGKS, the CF will be introduced later.

### 3.3. Reconstruction for the Boundary Cells

One ghost cell is created for each boundary face by mirror symmetry of the corresponding inner cells. The cell-averaged quantities can be assigned according to the boundary condition. Then the reconstruction for the inner cell can be determined. After obtaining the inner state (assume as $\tilde{\mathbf{W}}^r$) at a boundary Gaussian point, a ghost state (assume as $\tilde{\mathbf{W}}^l$) can be assigned according to boundary condition under local coordinates. There is a possible discontinuity between $\tilde{\mathbf{W}}^l$ and $\tilde{\mathbf{W}}^r$. The ghost state setting for isothermal wall with Maxwellian reflection is given as follows.

- The slip wall assumption allows a discontinuity in velocities at the cell interface, and the corresponding gas distribution function is $f = f_0^r|_{u_1<0} + f_0^l|_{u_1>0}$, where the inner non-equilibrium state is

$$f_0^r = \mathrm{e}^{-t/\tau}g^r[1 - \tau(a_{x_i}^r u_i + A^r) - t a_{x_i}^r u_i].$$

  A time-independent Maxwellian distribution $f_0^l(\mathbf{0}, \mathbf{u}, t) = \rho^l(\frac{\lambda^l}{\pi})\,\mathrm{e}^{-\lambda^l(\mathbf{u}^2+\xi^2)}$ is assumed in the ghost state with zero macroscopic velocities $U_i^l = 0$, a fixed temperature $T^l = 1/(2R\lambda^l)$, where $R$ is gas constant, and zero derivatives of the conservative variables $\partial\mathbf{W}^l = 0$.
- Then, $\rho^l$ is determined by no penetration constraint through the solid wall, which is obtained by solving the zero mass flux $\int u_1 f\,\mathrm{d}\Xi = \int u_1(f_0^r|_{u_1<0} + f_0^l|_{u_1>0})\,\mathrm{d}\Xi = 0$.
- The conservative variables $\mathbf{W}^{n+1}$ and the fluxes $\mathbf{F}^{n+1}$ are given by the above $f$ at the boundary.

The settings for the slipwall, non-slip adiabatic wall, and non-slip isothermal wall are described in Ji et al. (2021b).

### 3.4. Reconstruction of Equilibrium State

The reconstructions for the non-equilibrium states have the same spatial order of accuracy and can be used to get the equilibrium state $g^c, g_{x_i}^c$ directly by a suitable average of $g^{l,r}, g_{x_i}^{l,r}$. To be consistent with the construction of $g^c$, a kinetic-based weighting method is adopted

$$\begin{aligned}\int\boldsymbol{\psi}g^c\,\mathrm{d}\Xi = \mathbf{W}^c &= \int_{u>0}\boldsymbol{\psi}g^l\,\mathrm{d}\Xi + \int_{u<0}\boldsymbol{\psi}g^r\,\mathrm{d}\Xi,\\ \int\boldsymbol{\psi}g_{x_i}^c\,\mathrm{d}\Xi = \mathbf{W}_{x_i}^c &= \int_{u>0}\boldsymbol{\psi}g_{x_i}^l\,\mathrm{d}\Xi + \int_{u<0}\boldsymbol{\psi}g_{x_i}^r\,\mathrm{d}\Xi.\end{aligned} \tag{19}$$

The data for this method has compact support. In programming, this procedure is included inside the subroutine of the gas distribution function, since it is performed at the local coordinate. Thus, it is also cache-friendly. This method has been validated in the previous CGKS (Ji et al. 2021a, 2021b). In this way, all components of the microscopic slopes in Equation (5) can be determined.

### 3.5. Compression Factor for Cell-Averaged Gradient

A necessary condition for the divergence theorem is the smoothness of the conservative variables inside the targeted cell. Once a discontinuity exists within the targeted cell, the cell-averaged gradients obtained by Equation (10) are not reliable. Therefore, one idea to improve the robustness of the CGKS is to make the absolute value of the cell-averaged gradients be small enough near discontinuities. Then, the WENO reconstruction in Equation (18) will reduce to the first order of accuracy at next step. In this paper, the CF $\alpha_c$ at targeted cell $\Omega_0$ is defined as

$$\alpha_c = \prod_{i=0}^{N_f} \prod_{k=0}^{M_i} \alpha_{i,k}, \quad \alpha_c \in (0, 1], \tag{20}$$

where $\alpha_{i,k}$ is the gradient compression factor for the $k$th Gaussian point at the interface $i$ around $\Omega_0$. Then, the updated slope is then modified as

$$\tilde{\mathbf{W}}_{x_i}^{n+1} = \alpha_c \mathbf{W}_{x_i}^{n+1},$$

The gradient compression factor $\alpha$ at a Gaussian point is defined as

$$\alpha = \frac{1}{1 + [\delta Q/(\delta \overline{Q} + \epsilon)]^{K_s} F}. \tag{21}$$

$\delta Q$ is the absolute difference of the reconstructed left and right values at a cell interface. In smooth region, $\delta Q$ is on the order $O(\Delta x^{p+1})$. $\delta \bar{Q}$ the absolute difference of the left and right cell-averaged values around a cell interface. In smooth region, $\delta \bar{Q}$ is on the order $O(\Delta x)$. $F$ is given as

$$F = [C_1 D_p + C_2 (D_{Ma,2} + D_{Ma,3})]^{K_t}, \quad F \in [0, \infty),$$

$$D_p = \left| \frac{p^l - p^r}{p^l + p^r} \right|,$$

$$D_{Ma,2} = \left| \frac{{Ma_2}^l - {Ma_2}^r}{{Ma_2}^l + {Ma_2}^r + \epsilon} \right|,$$

$$D_{Ma,3} = \left| \frac{{Ma_3}^l - {Ma_3}^r}{{Ma_3}^l + {Ma_3}^r + \epsilon} \right|,$$

where $D_p$ is the related pressure difference, $Ma_2$ and $Ma_3$ are the Mach differences in two tangential directions.

The above parameters are selected based on the following criteria.

(1) $\delta Q/(\delta \overline{Q}) \to O(1)$ near discontinuities, such as shocks and shears.
(2) $F$ is a weighting factor for $\delta Q/(\delta \overline{Q})$. It can avoid excessive numerical dissipation around local extrema for smooth flow $\delta \overline{Q} \to 0$ and $\delta Q/(\delta \overline{Q}) \to +\infty$. $F$ approaches 0 for smooth flow and to a constant around discontinuities.
(3) The pressure difference $D_p$ and the Mach differences in two tangential directions $Ma_2$ and $Ma_3$ in $F$ are used to capture strong shock and shear layer in three-dimensional simulations.
(4) A large $K_s$ and $K_t$ corresponds to small numerical dissipations. At the same time, $K_s$ should not be below 2 from the accuracy requirement. Numerical dissipations increases in the increment of $C_1$ and $C_2$.
(5) Similar numerical performances can be obtained by taking density, pressure, or entropy for $Q$. The values $C_1 = 0.5 \sim 2$, $C_2 = 0.1 \sim 1$, $K_t = 2 \sim 6$ are suggested to balance robustness and accuracy of the scheme. In the current paper, $Q$ is defined by density, and $K_s = 2$, $C_1 = 1.5$, $C_2 = 0.2$, $K_t = 4$ are used in the simulations.

**Remark 3.1:** When the flow around $\Omega_0$ is smooth,

$$[\delta Q/(\delta \overline{Q}) + \epsilon)]^{K_s} = O(\Delta x)^{pK_s},$$
$$F = [C_1 O(\Delta x)^{p+1} + C_2 O(\Delta x)^{p+1}]^{K_t}$$
$$= O(\Delta x)^{(p+1)K_t},$$

where $p$ is the order of the reconstructed polynomial. Thus, recall Equations (21) and (20),

$$\alpha_{i,k} \to 1 + O(\Delta x)^{pK_s + (p+1)K_t},$$
$$\alpha_c = \prod_{i=0}^{N_f} \prod_{k=0}^{M_i} \alpha_{i,k} \to 1 + O(\Delta x)^{pK_s + (p+1)K_t},$$

which gives $\alpha_c \sim 1$ for smooth flow.

When the flow around $\Omega_0$ contains discontinuity, there are

$$[\delta Q/(\delta \overline{Q}) + \epsilon)]^{K_s} \to O(1),$$
$$D_p \to 1, \quad D_{Ma,2} \to 1, \quad D_{Ma,3} \to 1,$$
$$F \to (C_1 + C_2)^{K_t}.$$

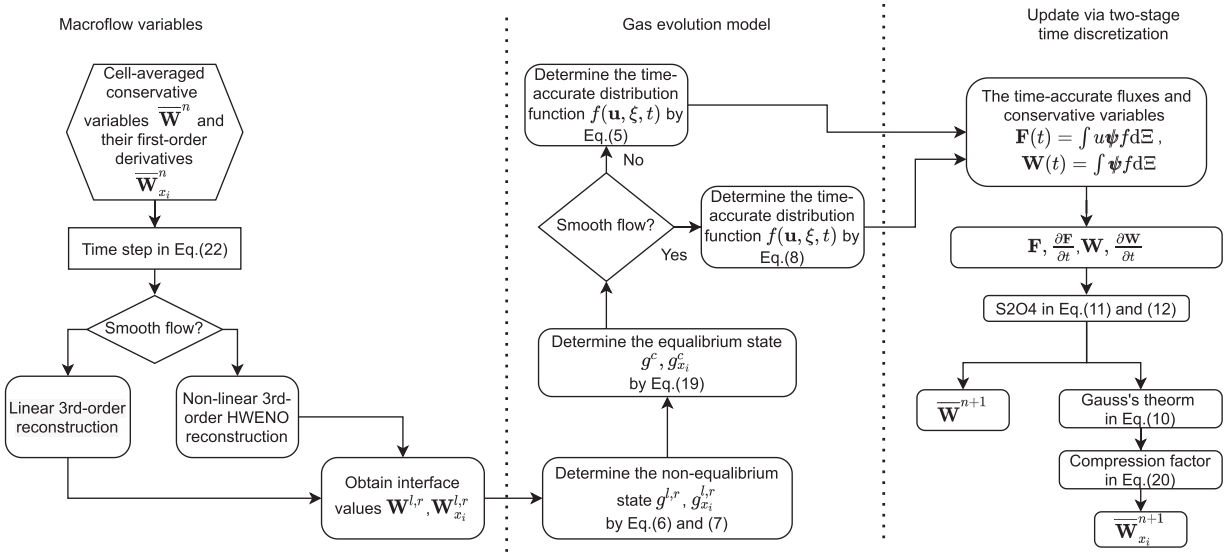


**Figure 2.** The brief algorithm of the CGKS.

As a result,

$$\alpha_{i,k} \to \frac{1}{1+|O(1)|},$$

$$\alpha_c = \prod_{i=0}^{N_f}\prod_{k=0}^{M_i}\alpha_{i,k} \to \frac{1}{1+|O(1)|}.$$

So, $\alpha_c$ can approach to 0 for discontinuous flow.

## 4. Numerical Examples

In this section, numerical tests will be presented to validate the proposed scheme. The time step is determined by

$$\Delta t = C_{CFL}\mathrm{Min}\left(\frac{\Delta r_i}{\|\mathbf{U}_i\|+(a_s)_i}, \frac{(\Delta r_i)^2}{3\nu_i}\right), \qquad (22)$$

where $C_{CFL}$ is the CFL number, and $\|\mathbf{U}_i\|$, $(a_s)_i$, and $\nu_i = (\mu/\rho)_i$ are the magnitude of velocities, sound speed, and kinematic viscosity coefficient for cell i. The $\Delta r_i$ is taken as

$$\Delta r_i = \frac{3|\Omega_i|}{\sum|\Gamma_{ip}|},$$

for a tetrahedron or pyramid, and

$$\Delta r_i = \frac{|\Omega_i|}{\max|\Gamma_{ip}|},$$

for a hexahedron or prism. The CFL number is taken as 0.5 if no specified. An algorithm flowchart of the CGKS is given in Figure 2. In the present work, the WENO reconstruction based on the conservative variables and the complete flux in Equation (5) are adopted in the test cases without using the CF if no specified.

### 4.1. 3-D Sinusoidal Wave Propagation

The initial condition for the advection of density perturbation is given as

$$\rho(x,y,z) = 1+0.2\sin(\pi(x+y+z)),$$
$$\mathbf{U}(x,y,z) = (1,1,1), \quad p(x,y,z) = 1,$$

within a cubic domain $[0,2]\times[0,2]\times[0,2]$. A series of sequentially refined hexahedral meshes and hybrid meshes are used in the test, as shown in Figure 3. With the periodic boundary condition in all directions, the analytic solution is

$$\rho(x,y,z,t) = 1+0.2\sin(\pi(x+y+z-t)),$$
$$\mathbf{U}(x,y,z) = (1,1,1), \quad p(x,y,z,t) = 1.$$

The flow is inviscid and the collision time $\tau$ is 0. The $L^1$, $L^2$ and $L^\infty$ errors and the corresponding orders with linear weights at $t=2$ under both meshes are given in Tables 1 and 2. The results with non-linear Z-type weights for uniform meshes are given in Table 3. Expected accuracy is achieved for the above cases. Then, the results for the CGKS with the CF are listed in Table 4. In comparison with the results without the CF, the absolute errors are slightly increased as shown in Table 5. The same conclusion can be drawn for the

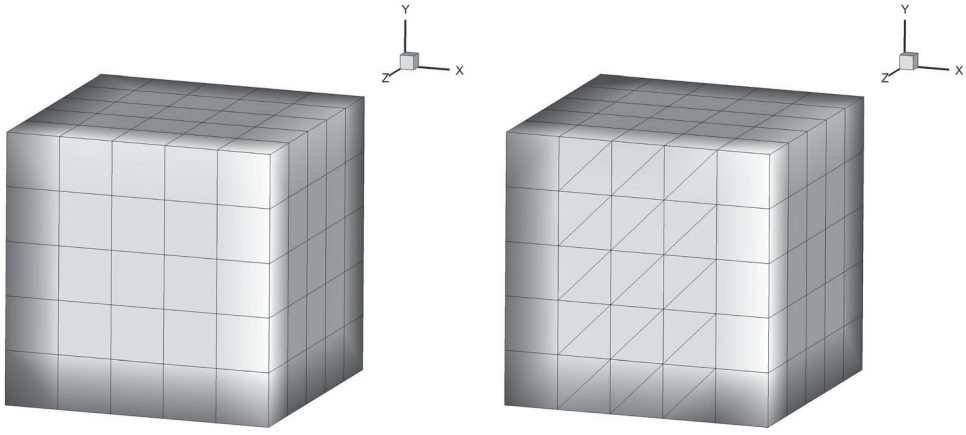


**Figure 3.** Mesh sample for the 3D sin-wave propagation. Left: hexahedral mesh. Right: Hybrid mesh.

**Table 1.** Accuracy test for the 3D sin-wave propagation by the linear third-order compact reconstruction.

| Mesh number | C $L^1$ error | C Order | C $L^2$ error | C Order | C $L^\infty$ error | C Order |
|---|---|---|---|---|---|---|
| $5^3$ | 8.572800e−02 | | 9.508770e−02 | | 1.324228e−01 | |
| $10^3$ | 2.199962e−02 | 1.96 | 2.441038e−02 | 1.96 | 3.420145e−02 | 1.95 |
| $20^3$ | 3.083322e−03 | 2.83 | 3.431975e−03 | 2.83 | 5.052936e−03 | 2.76 |
| $40^3$ | 3.948944e−04 | 2.96 | 4.377654e−04 | 2.97 | 6.581416e−04 | 2.94 |

Note: Uniform hexahedral mesh.

**Table 2.** Accuracy test for the 3D sin-wave propagation by the linear third-order compact reconstruction.

| Mesh number | $L^1$ error | Order | $L^2$ error | Order | $L^\infty$ error | Order |
|---|---|---|---|---|---|---|
| $1.6 \times 5^3$ | 9.697442e−02 | | 1.080211e−01 | | 1.512287e−01 | |
| $1.6 \times 10^3$ | 2.821966e−02 | 1.78 | 3.151973e−02 | 1.77 | 4.422013e−02 | 1.77 |
| $1.6 \times 20^3$ | 4.036691e−03 | 2.81 | 4.496854e−03 | 2.81 | 6.650040e−03 | 2.73 |
| $1.6 \times 40^3$ | 5.168948e−04 | 2.97 | 5.729851e−04 | 2.97 | 8.596728e−04 | 2.95 |

Note: Hybrid mesh.

**Table 3.** Accuracy test for the 3D sin-wave propagation by the third-order compact WENO reconstruction with $d_0 : d_1 : d_2 = 100 : 1 : 6$.

| Mesh number | $L^1$ error | Order | $L^2$ error | Order | $L^\infty$ error | Order |
|---|---|---|---|---|---|---|
| $5^3$ | 9.307715e−02 | | 1.026267e−01 | | 1.431789e−01 | |
| $10^3$ | 1.782439e−02 | 2.38 | 2.040047e−02 | 2.33 | 3.581868e−02 | 2.00 |
| $20^3$ | 2.988300e−03 | 2.58 | 3.592716e−03 | 2.51 | 9.255122e−03 | 1.96 |
| $40^3$ | 4.108034e−04 | 2.86 | 5.008456e−04 | 2.84 | 1.114581e−03 | 3.05 |

Note: Uniform hexahedral mesh.

**Table 4.** Accuracy test for the 3D sin-wave propagation by the third-order compact WENO reconstruction with $d_0 : d_1 : d_2 = 100 : 1 : 6$ and the CF.

| Mesh number | $L^1$ error | Order | $L^2$ error | Order | $L^\infty$ error | Order |
|---|---|---|---|---|---|---|
| $5^3$ | 9.177411e−02 | | 1.014747e−01 | | 1.421968e−01 | |
| $10^3$ | 1.783722e−02 | 2.36 | 2.041512e−02 | 2.31 | 3.586210e−02 | 1.99 |
| $20^3$ | 2.827416e−03 | 2.65 | 3.717858e−03 | 2.48 | 1.140440e−02 | 1.65 |
| $40^3$ | 4.073909e−04 | 2.80 | 5.042275e−04 | 2.88 | 1.228363e−03 | 3.21 |

Note: Uniform hexahedral mesh.

**Table 5.** Accuracy test for the 3D sin-wave propagation by the third-order compact WENO reconstruction with $d_0 : d_1 : d_2 = 100 : 1 : 6$ and the CF.

| Mesh number | $L^1$ error | Order | $L^2$ error | Order | $L^\infty$ error | Order |
|---|---|---|---|---|---|---|
| $1.6 \times 5^3$ | 9.835342e−02 | | 1.105509e−01 | | 1.534561e−01 | |
| $1.6 \times 10^3$ | 4.301722e−02 | 1.19 | 4.875222e−02 | 1.18 | 7.870885e−02 | 0.96 |
| $1.6 \times 20^3$ | 4.335145e−03 | 3.31 | 5.664078e−03 | 3.11 | 1.174496e−02 | 2.74 |
| $1.6 \times 40^3$ | 5.491532e−04 | 2.98 | 6.424909e−04 | 3.14 | 1.412450e−03 | 3.06 |

Note: Hybrid mesh.

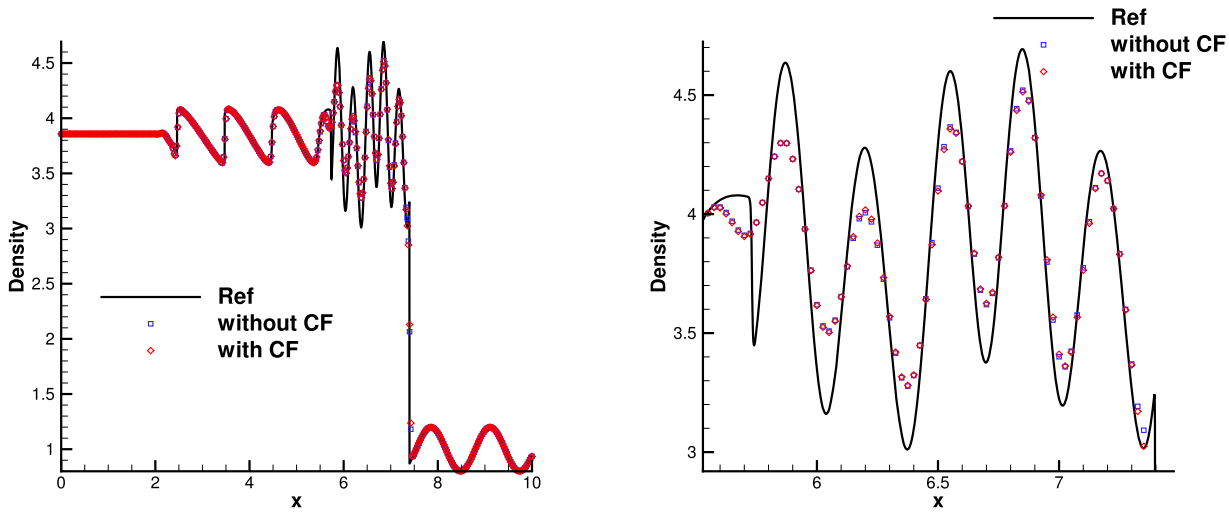


**Figure 4.** Shu–Osher problem. Mesh number: 400 × 2 × 2.

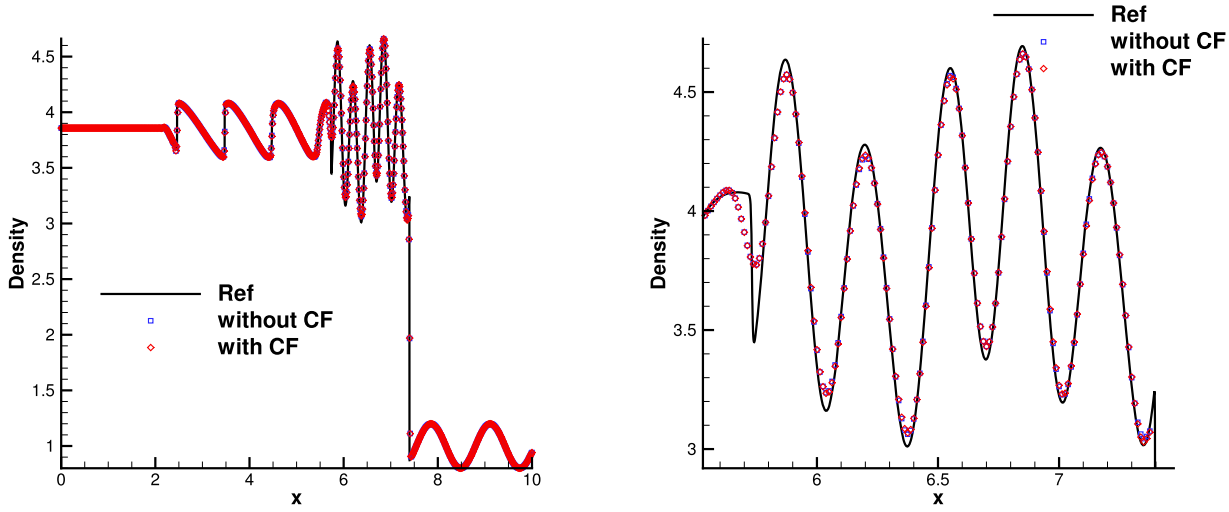


**Figure 5.** Shu–Osher problem. Mesh number: 800 × 2 × 2.

cases under hybrid meshes, as shown in Table 5. The third-order accuracy is kept for both cases.

### 4.2. Shu–Osher Problem

The initial condition for the Shu–Osher problem (Shu and Osher 1989) is

$$(\rho, U, p) = \begin{cases} (3.857134, 2.629369, 10.33333), & 0 < x \leq 1, \\ (1 + 0.2\sin(5x), 0, 1), & 1 < x < 10. \end{cases}$$

The flow is one-dimensional along the $x$-axis, and two uniform hexahedral meshes with a fixed length $L = 10$ in $x$-direction are used in the computation. The mesh sizes are $\Delta x = 1/40$ and $1/80$, respectively. The fixed wave profile is extended on the right while the non-reflecting boundary condition is given on the left. The computed density profiles and local enlargements for the Shu–Osher problem at $t = 1.8$ with both meshes are plotted in Figures 4 and 5. The CGKS with/without the CF can both resolve the linear wave nicely. To get a better understanding of the behaviour of the CF in this test, the distributions for the CF at $t = 1.8$ in each cell are plotted in Figure 6. It can be observed that the CF only takes effect near the normal shock. The results are also compared with the 1-D second-order GKS based on the van Leer limiter. A similar resolution can be

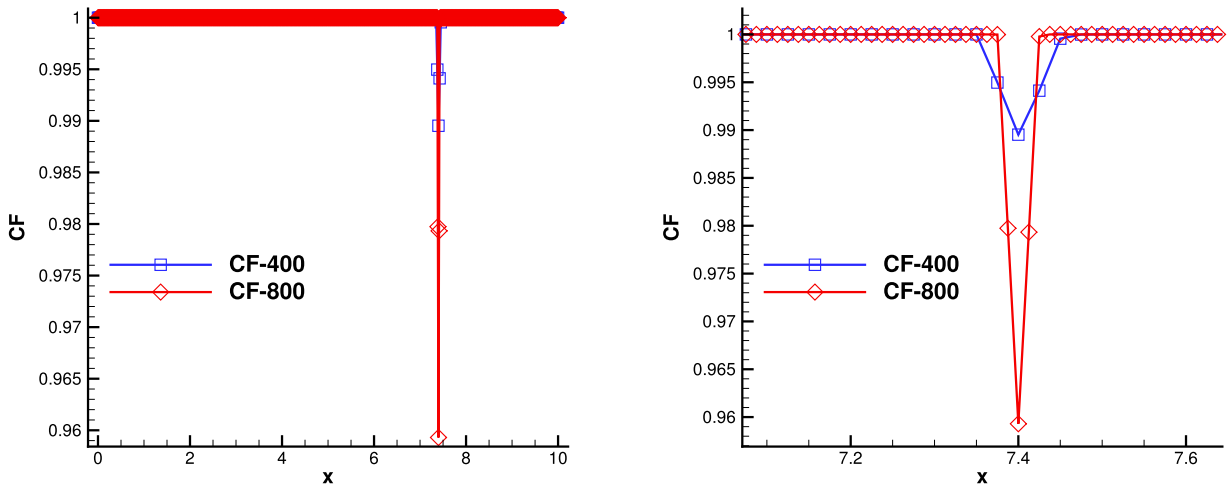


**Figure 6.** The CF distributions and their local enlargements in Shu–Osher problem.

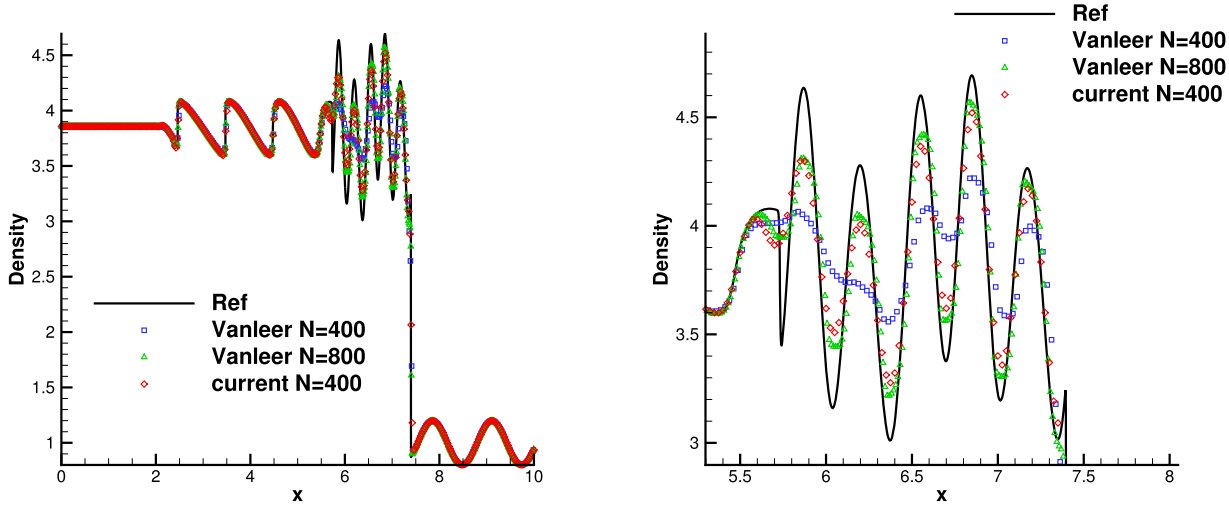


**Figure 7.** Shu–Osher problem from the current third-order CGKS and previous second-order GKS.

obtained by the current scheme with only half of the total mesh points used by a second-order method, as shown in Figure 7.

### 4.3. Laminar Boundary Layer

A laminar boundary layer over a flat plate with incoming Mach number $Ma = 0.15$ is simulated. The Reynolds number $Re = U_\infty L/\nu = 10^5$, where the characteristic length $L = 100$. The computational domain is shown in Figure 8, where the flat plate is placed at $x > 0$ and $y = 0$. Total $120 \times 35 \times 2$ hexahedral cells are used in a cuboid domain $[-30, 100] \times [0, 80] \times [0, 0.2]$ with a cell height $h = 0.1$ adjacent to the boundary. The adiabatic non-slip boundary condition is imposed on the plate and symmetric slip boundary condition is set in the front of the plate. The non-reflecting boundary condition based on the Riemann invariants is adopted for the other boundaries, where the free stream is set as $\rho_\infty = 1$, $p_\infty = 1/\gamma$. Since the flow is nearly incompressible, the smooth reconstruction and the simplified solver in Equation (8) are adopted to further reduce the numerical dissipation. The non-dimensional velocity U and V are given in Figure 9 at three selected locations. The wall distributions of the skin-fraction coefficients $C_f$ are also plotted, where the local Reynolds number $Re_x$ and the $C_f$ are defined as

$$Re_x = \frac{x}{L} Re, \quad C_f = \frac{\tau_{wall}}{\frac{1}{2}\rho_\infty U_\infty^2},$$

where $\tau_{wall}$ is the skin shear stress. The numerical results agree well with the Blasius solutions with a few mesh points at $x/L = 0.1$.

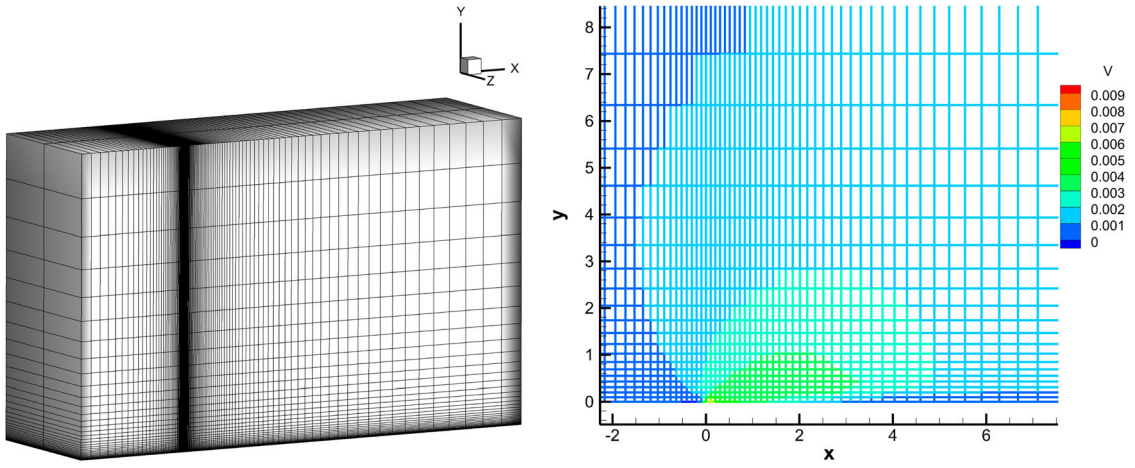


**Figure 8.** Laminar boundary layer. Left: mesh with 120 × 35 × 2 cells. Right: local enlargement coloured by V velocities.

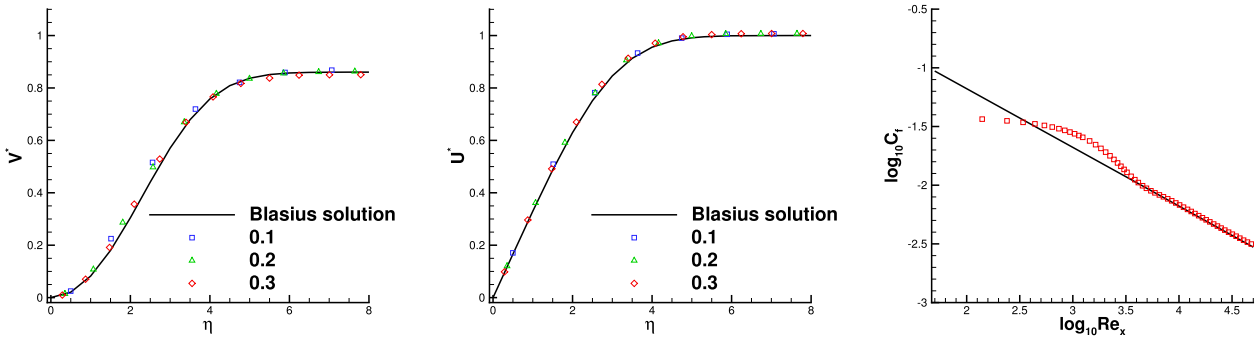


**Figure 9.** Laminar boundary layer. The velocities profiles and skin-frication coefficient.

### 4.4. Subsonic Viscous Flow Around a Cylinder at Re = 40

An incoming flow with Mach number $Ma = 0.15$ and Reynolds number $Re = 40$ based on the diameter of the cylinder $D = 1$ around a circular cylinder is simulated. The flow is smooth and the same setting as the boundary layer is adopted in the computation. The computational domain is shown in Figure 10, where total $241 \times 114 \times 2$ hexahedral cells are used in a cylindrical domain $D_{mesh} = 96.0$, $H_{mesh} = 0.1$ with a near-wall size $h = 1/96$. A steady and symmetrical separation bubble is located at the wake of the cylinder. Quantitative results including the drag and lift coefficients $C_D$, $C_L$, the wake length $L$, and the separation angle $\theta$, etc are listed in Table 6, which agree well with the experimental and numerical references (Tritton 1959; Coutanceau and Bouard 1977; Fan Zhang, Cheng, and Liu 2019). Furthermore, the quantities on the cylinder surface are extracted, including the surface pressure coefficient $C_p = \frac{p-p_\infty}{\frac{1}{2}\rho_\infty U_\infty^2}$, and the non-dimensional local tangential velocity gradient $\frac{2D}{U_\infty}\frac{\partial U_\tau}{\partial \eta}$, as shown in Figure 11. The $C_p$ from the current CGKS matches nicely with the experimental data (Grove, Shair, and Petersen 1964) and the analytical solution (Bharti, Chhabra, and Eswaran 2006). The tangential velocity gradient obtained by the current scheme is compared with those by the finite difference method (Braza, Chassaing, and Ha Minh 1986) and the direct DG method (Fan Zhang, Cheng, and Liu 2019).

### 4.5. Flow Passing Through a Sphere From Subsonic to Hypersonic Cases

Viscous flow over a sphere with a wide range of Mach numbers are tested below to validate the capability of the CGKS in different flow regions. The Reynolds numbers are based on the diameter of the sphere

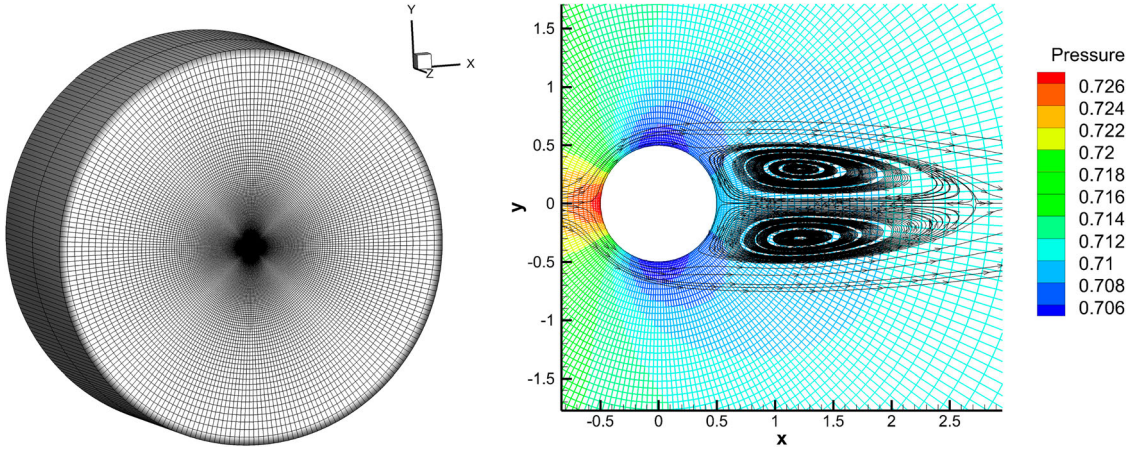


**Figure 10.** Circular cylinder: $Re = 40$. Left: mesh with $241 \times 114 \times 2$ cells. Right: local mesh distribution around cylinder coloured by pressure and streamline.

**Table 6.** Comparison of results for steady flow past a circular cylinder at $Re = 40$.

| Case | $C_D$ | $C_L$ | $L$ | Vortex Height | Vortex Width | $\theta$ |
|---|---|---|---|---|---|---|
| Experiment (Tritton 1959) | 1.46–1.56 | – | – | – | – | – |
| Experiment (Coutanceau and Bouard 1977) | – | – | 2.12 | 0.297 | 0.751 | 53.5° |
| DDG (Fan Zhang, Cheng, and Liu 2019) | 1.529 | – | 2.31 | – | – | – |
| Current | 1.525 | 3.3e−14 | 2.22 | 0.296 | 0.714 | 53.3° |

$D = 1$. The far-field condition is set at outside boundary of the domain with the free stream condition

$$(\rho, U, V, W, p)_\infty = \left(1, Ma, 0, 0, \frac{1}{\gamma}\right),$$

with $\gamma = 1.4$. For the subsonic cases, the smooth reconstruction and the simplified solver in Equation (8) are adopted to achieve a high resolution.

(a) *Subsonic case*: $Re = 118$, $Ma = 0.2535$.

A low-speed viscous flow passing through a sphere is tested first. In such case, a drag coefficient $C_D = 1$ was reported from the experiment in Taneda (1956). The surface of the sphere is set as non-slip and adiabatic. A hexahedral mesh is used and the first mesh off the wall has the size $h \approx 4.5 \times 10^{-2} D$, as shown in Figure 12. The Mach magnitude contour and the

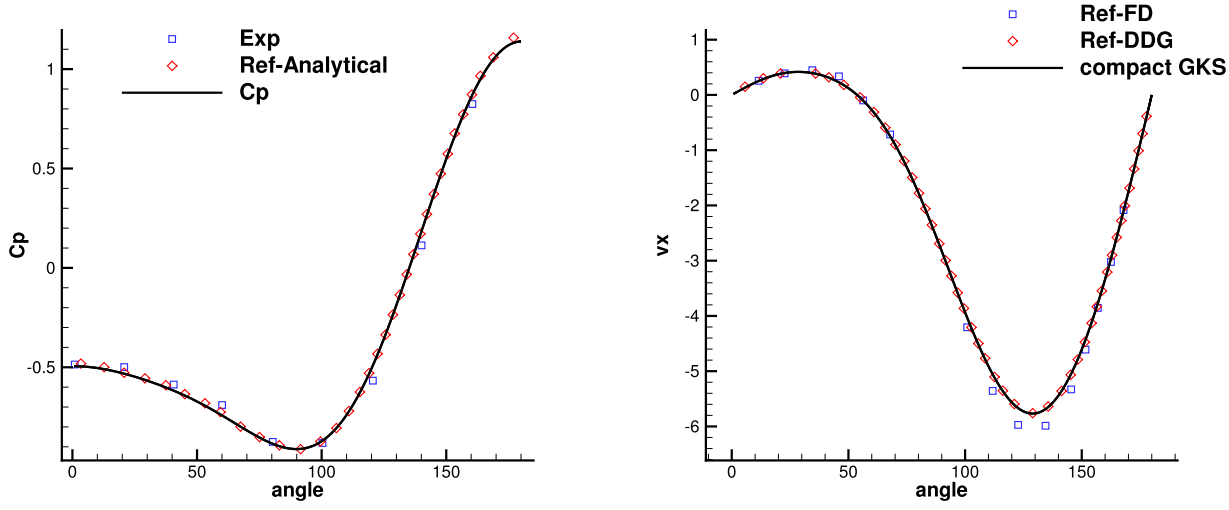


**Figure 11.** Circular cylinder: $Re = 40$. Left: surface pressure coefficient distribution. Right: surface local tangential velocity gradient distributions.

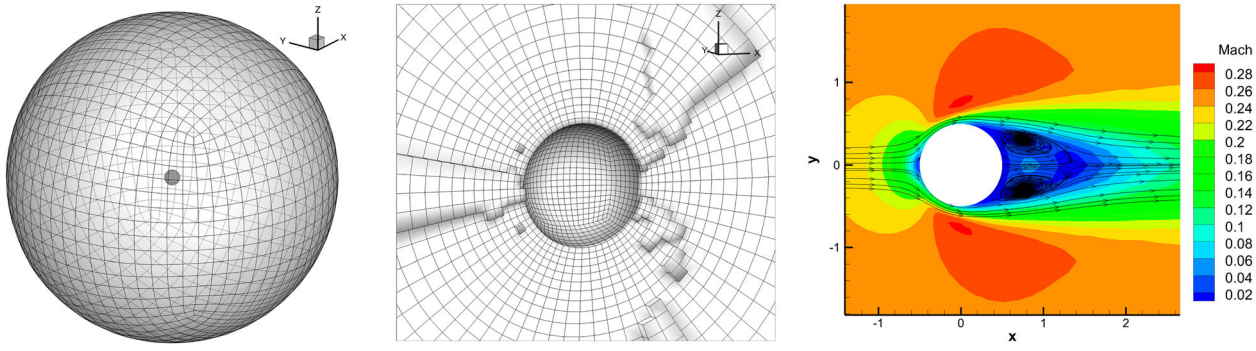


**Figure 12.** Flow passing through a sphere. $Ma = 0.2535$. $Re = 118$. Mesh number: 50,688.

**Table 7.** Results from different compact schemes for the viscous flow over a sphere.

| Scheme | Mesh number | $C_D$ | $\theta$ | $L$ | $C_L$ |
|---|---|---|---|---|---|
| Experiment (Taneda 1956) | – | 1.0 | 151 | 1.07 | – |
| Third-order DDG (Cheng et al. 2017) | 160,868 | 1.016 | 123.7 | 0.96 | – |
| Fourth-order VFV (Qian Wang 2017) | 458,915 | 1.014 | – | – | 2.0e−5 |
| Current | 50,688 | 1.016 | 124.7 | 0.86 | 3.6e−3 |

streamline around the sphere are presented as well. The quantitative results are given in Table 7, including the drag coefficient $C_D$, the separation angle $\theta$, and the closed wake length $L$, as defined in Ji et al. (2021a). The drag coefficient is very close to those by other methods even with a much coarser mesh.

(b) *Subsonic case*: $Re = 300$, $Ma = 0.3$.

The flow is unsteady in this case and the hairpin vortex structure will be formed in the wake region of the sphere. A hexahedral mesh is used and the whole computation domain has a dimension $[-10, 40] \times [-10, 10] \times [-10, 10]$ with a near-wall size $h \approx \frac{1}{100}D$ along the radial direction and $h \approx \frac{1}{128}D$ along the circumferential direction, as shown in Figure 13. The current scheme can resolve the vortex shedding nicely, as shown in Figure 14. The drag and lift coefficients change in a single frequency mode with time increasing, as shown in Figure 15. The frequency and averaged drag coefficient agree well with the reference data, as listed in Table 8.

(c) *Transonic case*: $Re = 300$, $Ma = 0.95$.

A hybrid unstructured mesh with total 515, 453 cells is used in the computation, as shown in Figure 16. The first grid off the wall is $1 \times 10^{-2}D$ while 128 cells are distributed along the circumferential direction. The non-reflective boundary is adopted on the outside boundary with a dimension $[-8, 16] \times [-8, 8] \times [-8, 8]$. The mesh is refined at the wake of the sphere where a long separation bubble is formed, as shown in Figure 17. The pressure distribution is also given in Figure 17, where the weak shock can be observed. Quantitative results are compared with the benchmark solutions in Nagata et al. (2016), where the $C_d$ and $\theta$ agree well with each other, as shown in Table 9.

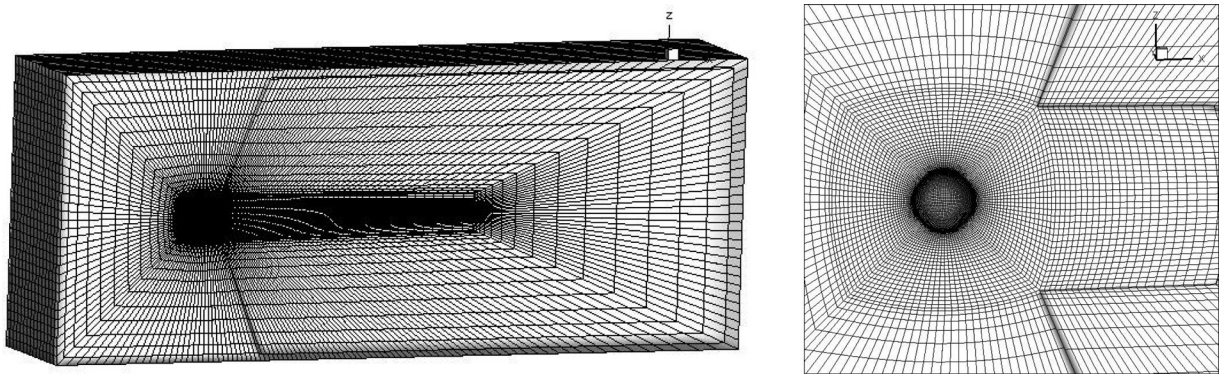

**Figure 13.** Flow passing through a sphere. $Ma = 0.3$. $Re = 300$. Mesh number: 479,232.

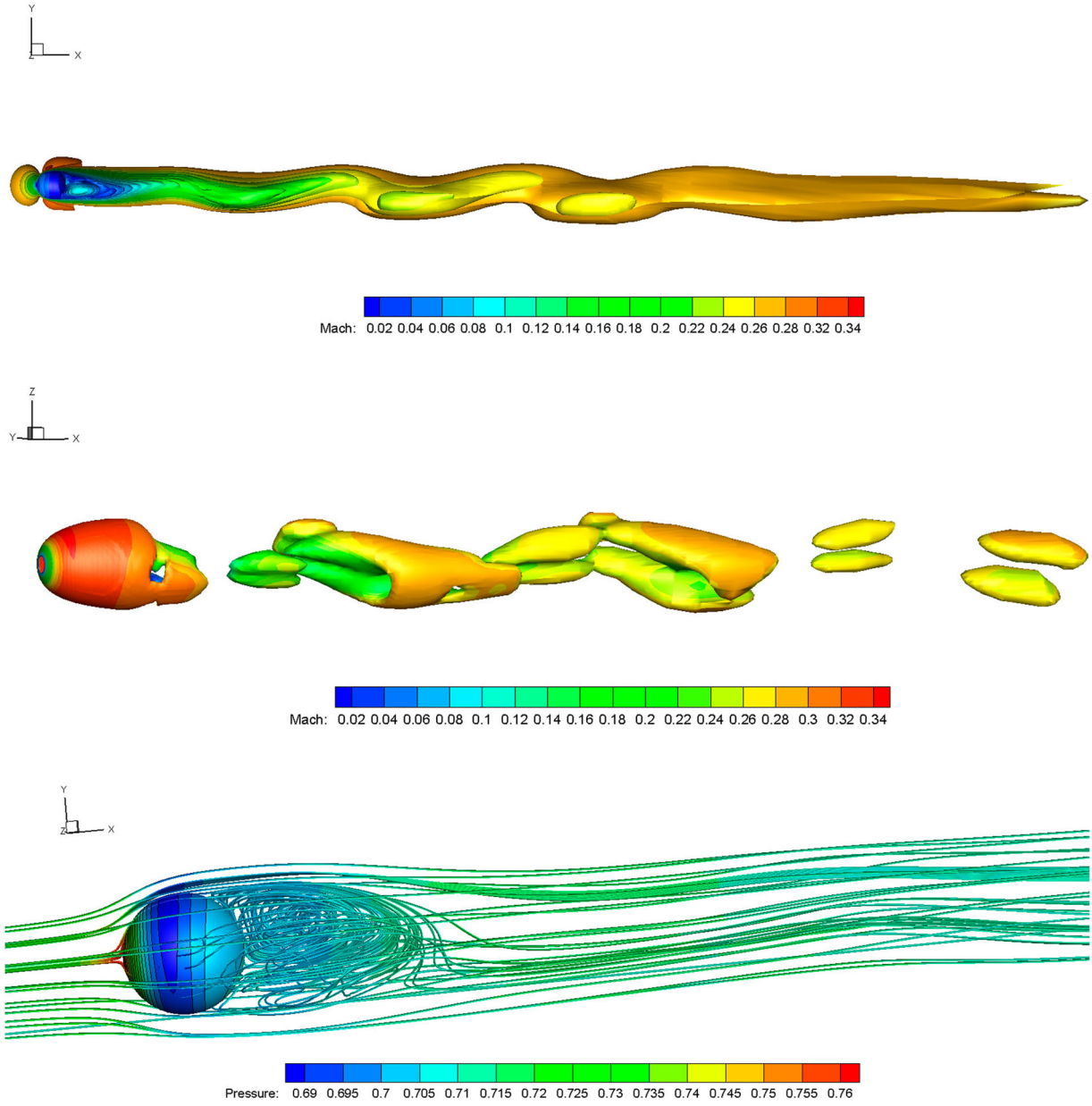


**Figure 14.** Flow passing through a sphere. $Ma = 0.3$. $Re = 300$. Top: Iso-surface of the Mach number. Middle: Iso-surface of the Q criterion $Q = 5 \times 10^{-4}$ coloured by Mach number. Bottom: 3-D streamline coloured by pressure.

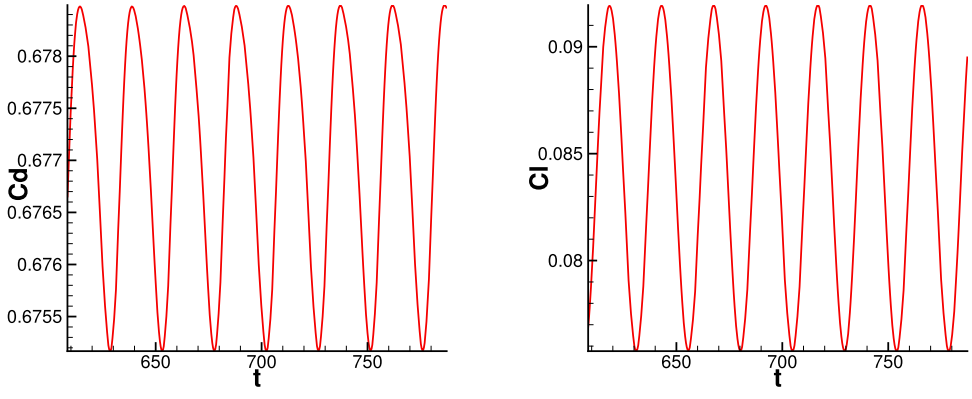


**Figure 15.** The time history of the $C_D$ and $C_L$. $Ma = 0.3$. $Re = 300$.

**Table 8.** Results from different schemes for the supersonic viscous flow over a sphere.

| Scheme | Mesh Number | $C_D$ | $\Delta C_D$ | $\lvert C_L \rvert$ | $\Delta C_L$ | St |
|---|---|---|---|---|---|---|
| Third-order k-exact (Wanai Li 2014) | 2,065,612 | 0.674 | 0.003 | 0.055 | 0.013 | 0.133 |
| Current | 479,232 | 0.677 | 0.003 | 0.084 | 0.016 | 0.135 |

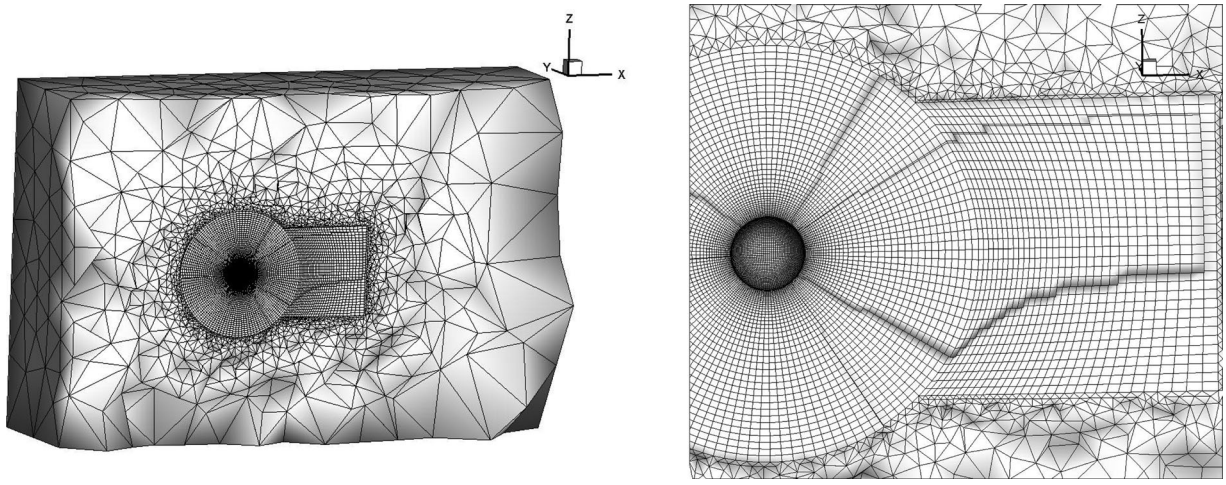


**Figure 16.** Flow passing through a sphere. $Ma = 0.95$. $Re = 300$. Mesh number: 515,453.

**Table 9.** Results from CGKS and WENO6 (Nagata et al. 2016) for the transonic flow over a sphere.

| Scheme | Mesh Number | Cd | $\theta$ | L |
|---|---|---|---|---|
| WENO6 (Nagata et al. 2016) | 909,072 | 0.968 | 111.5 | 3.48 |
| Current | 515,453 | 0.950 | 112.7 | 3.30 |

Note: $Ma = 0.95$. $Re = 300$.

(d) *Supersonic case*: $Re = 300$, $Ma = 2.0$.

To evaluate the effect of the CF for the supersonic flow, a viscous flow around a sphere with $Ma = 2.0$ is tested. The non-slip adiabatic boundary condition is imposed on the surface of the sphere. The same computational mesh for case (a) is used here. To pass this case, an initial field calculated by the first-order kinetic method (Xu 2014) has to be used for the CGKS without CF. But, it is not necessary for the CGKS with CF. The numerical results obtained by the CGKS with/without the CF are shown in Figure 18. Almost identical contours and streamlines are obtained. Quantitative comparisons are listed in Table 10. Very close results are obtained by the CGKS with/without the CF. And they have good agreements with those given by Nagata et al. (2016). The test shows that the current CF can improve the robustness of the CGKS while keeping the same level of accuracy in supersonic region. The time-dependent CF distributions are given in Figures 19 and 20. At the very early step (Step 2), the slopes are modified near the tail of the sphere, where a rarefaction wave is formed instantly. Then, the region with a small CF gradually moves to the front of the sphere, where the bow shock is formed. Finally, there is almost no region with a CF

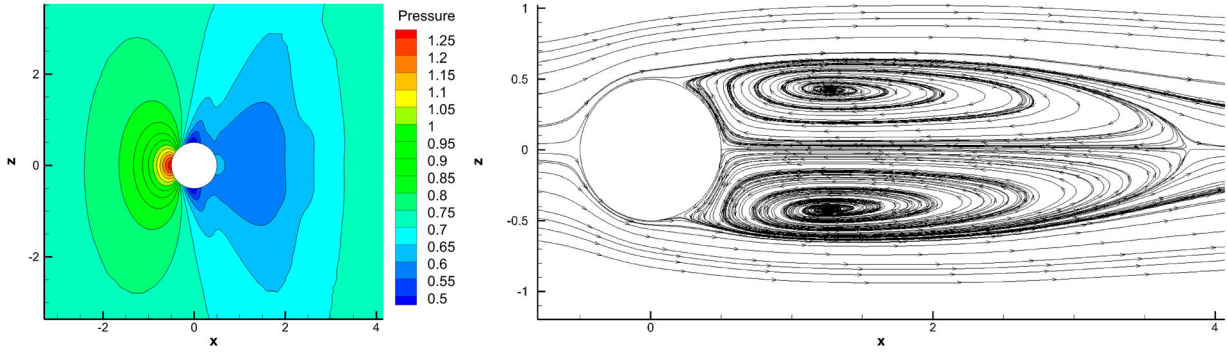


**Figure 17.** Flow passing through a sphere. $Ma = 0.95$. $Re = 300$.

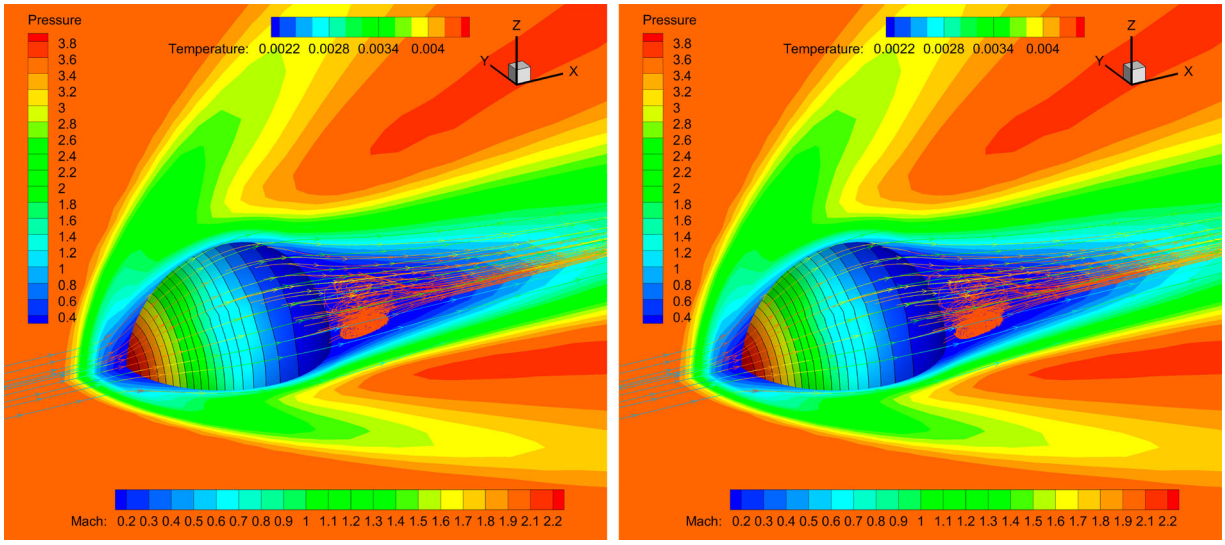


**Figure 18.** Flow passing through a sphere. $Ma = 2$. $Re = 300$. Left: without the CF. Right: with the CF.

**Table 10.** Results from CGKS with and without CF and WENO6 for the flow over a sphere at $Ma = 2, Re = 300$.

| Scheme | Mesh Number | Cd | $\theta$ | L | Shock stand-off |
|---|---|---|---|---|---|
| WENO6 (Nagata et al. 2016) | 909,072 | 1.386 | 150.9 | 0.38 | 0.21 |
| CGKS without CF | 50,688 | 1.368 | 148.5 | 0.45 | 0.28–0.31 |
| CGKS with CF | 50,688 | 1.368 | 149.2 | 0.45 | 0.28–0.31 |

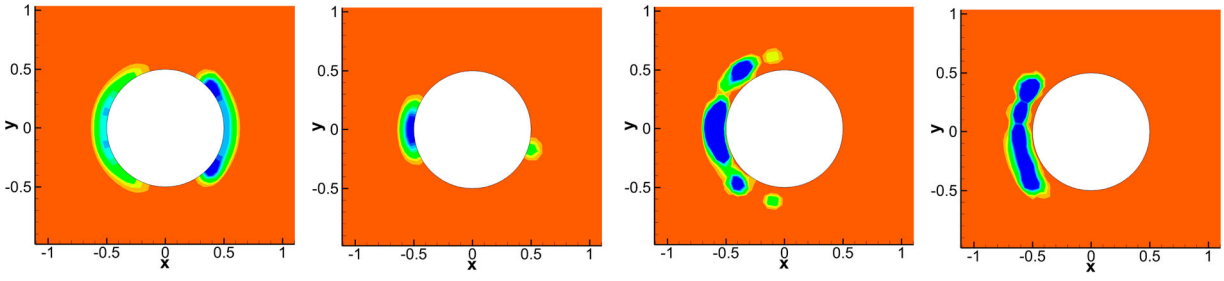

**Figure 19.** The CF distributions at step 2, 10, 20, 30 (from left to right).

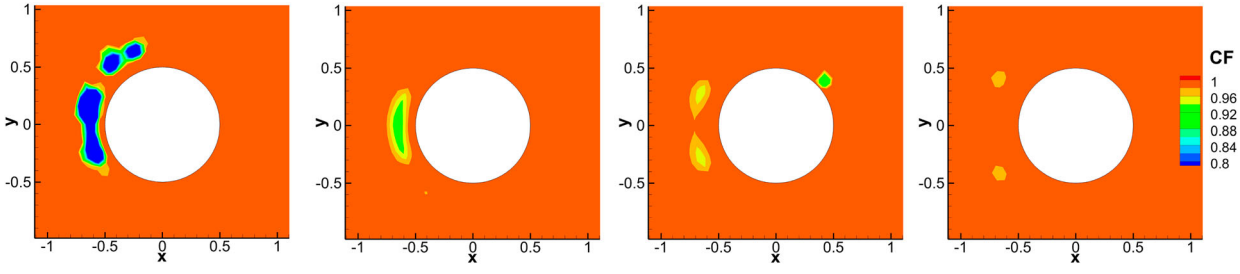


**Figure 20.** The CF distributions at step 40, 50, 100, 1000 (from left to right).

value less than 0.98 when approaching to the steady state solution.

(e) *Hypersonic case*: $Re = 300$, $Ma = 5.0$.

The $Ma = 5$ flow passing through a sphere is considered here. The Reynolds number is still set as $Re = 300$. The isothermal wall with Maxwellian reflection described in Subsection 3.3 is adopted on the surface of the sphere. The same computational mesh for case (a) is used here. With the CF, the CGKS can safely pass this stringent test. The Mach contours

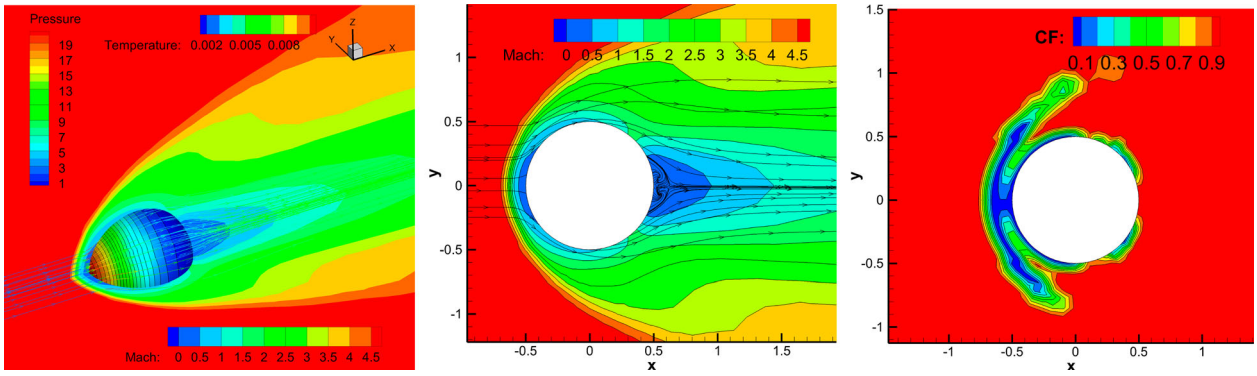


**Figure 21.** Flow passing through a sphere $Ma = 5$. $Re = 300$. Left: the surface of the sphere is coloured by pressure and the streamline is coloured by temperature. Middle: Mach number distribution. Right: the CF distribution.

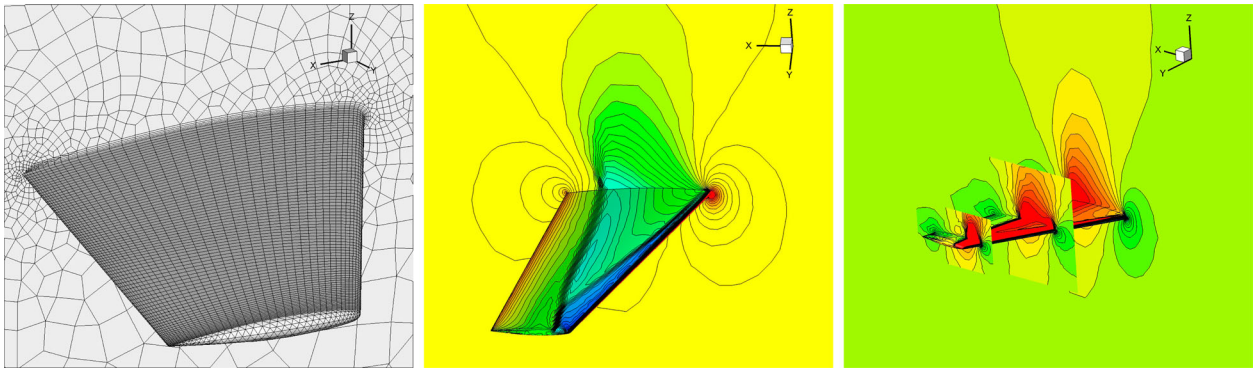

**Figure 22.** Transonic flow over an inviscid ONERA M6 wing under Mesh I. $Ma = 0.8935$. $AOA = 3.06^{\circ}$. Mesh: 210,663 cells.

and streamlines in both 2-D and 3-D views are presented in Figure 21. Only a tiny recirculation region is formed. In addition, the CF distribution in Figure 21 shows that the cell-averaged slopes are mostly modified near the wall and the bow shock. The minimum CF is $3 \times 10^{-29}$.

### 4.6. Transonic Inviscid ONERA M6 Wing

The transonic flow passing through the ONERA M6 wing is tested, as a validation case for compressible external flow. Experimental data are provided in Schmitt (1979) at a high Reynolds number. Instead of the simulation with a high Reynolds number in the experiment (Schmitt 1979), here an inviscid case reported in Liu et al. (2020) is simulated. The incoming Mach number is $Ma = 0.8395$ and the angle of attack is $AOA = 3.06^{\circ}$. The wing is hung on a slipwall, and the Riemann boundaries are applied 10 times of the root chord length away from the wing. A hybrid unstructured mesh with a near-wall size $h \approx 2e{-}3$ is used in the computation, as shown in Figure 22. The surface pressure distribution and Mach slices at different wing sections under are presented in Figure 22. The 'Lambda' shock is well resolved. Quantitative comparisons on the pressure distributions for six different locations on the wing are given in Figure 23, which show the CGKS can give a rough prediction for the real physical flow in this case.

### 4.7. Hypersonic Space Vehicle

A space vehicle model is considered to test the robustness of the proposed scheme for the hypersonic viscous flow. The initial condition is taken as suggested in Chen, Zhu, and Xu (2020), which has $Ma = 10$ and $AOA = 20^{\circ}$. The Reynolds number is chosen as 14,289 based on the vehicle's total length, which yields a Knudsen number $Kn = 10^{-3}$. Thus, the flow is in a transition regime and the isothermal wall with Maxwellian reflection described in Subsection 3.3 is applied on the vehicle's surface. The surface mesh is given in Figure 24. The density and pressure distributions are shown in Figure 25. The Mach distributions and streamlines are also plotted in Figure 26. The slip velocities can be observed on the surface of the space vehicle.

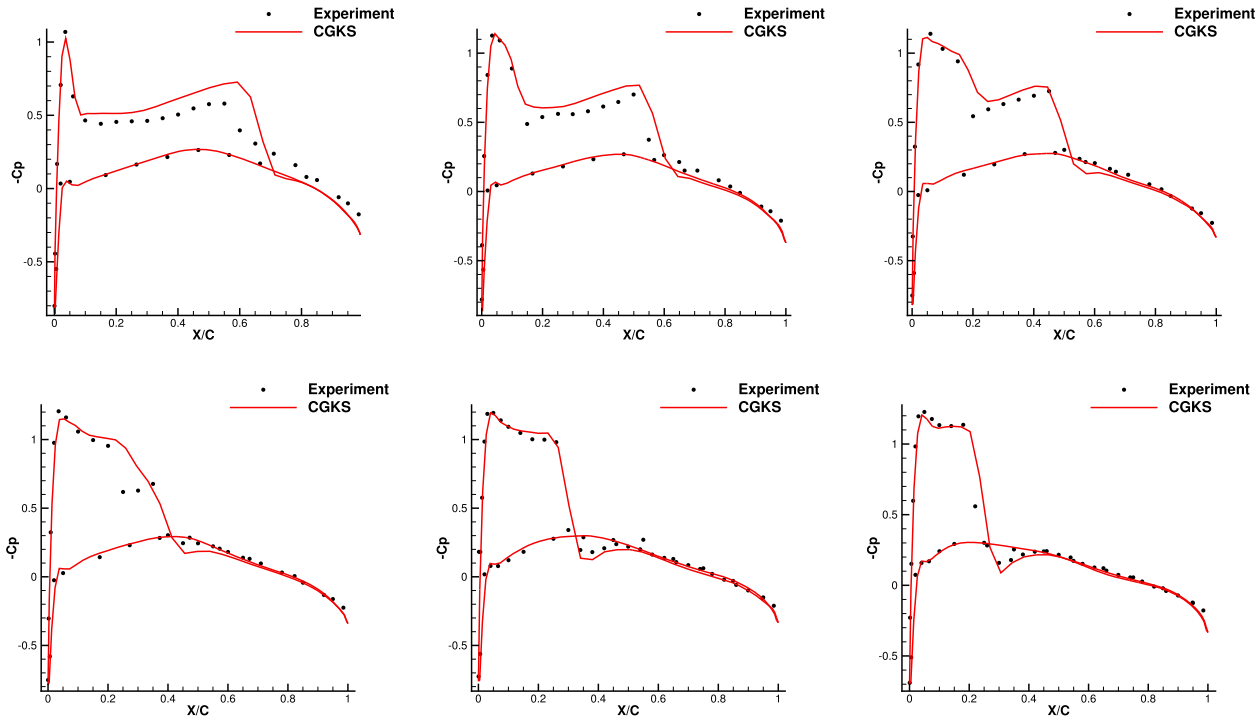


**Figure 23.** Pressure distributions at different semi-span locations Y/B on the ONERA M6 wing. $Ma = 0.8935$. $AOA = 3.06^{\circ}$. Top: $Y/B =$ 0.20, 0.44, 0.65 from left to right. Bottom: $Y/B = 0.80, 0.90, 0.95$ from left to right.

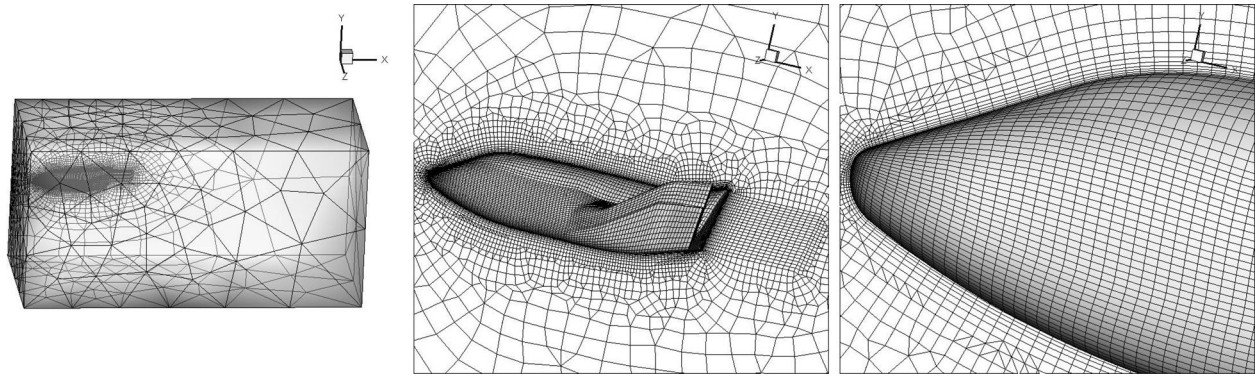

**Figure 24.** Mesh distribution around a space vehicle. Mesh number: 246,558.

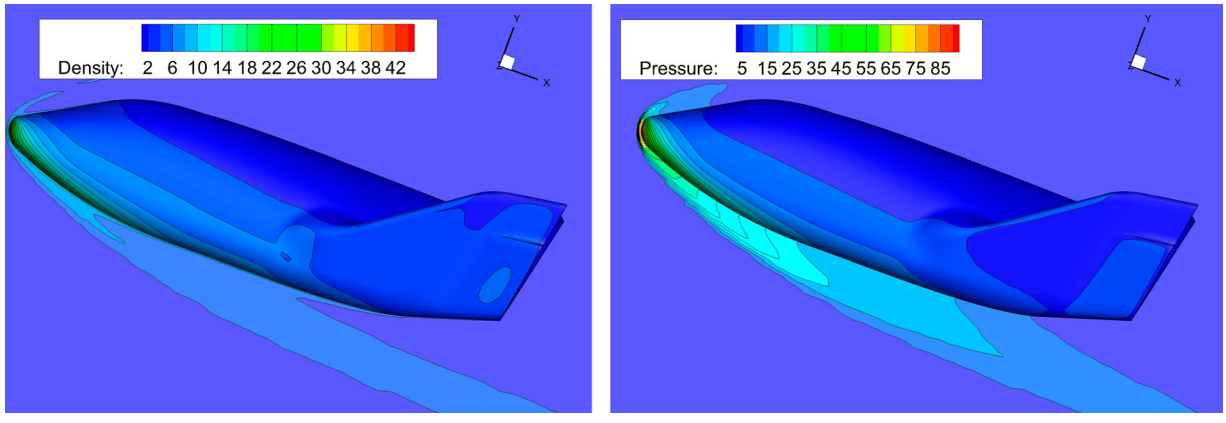


**Figure 25.** Density and pressure distributions around the space vehicle.

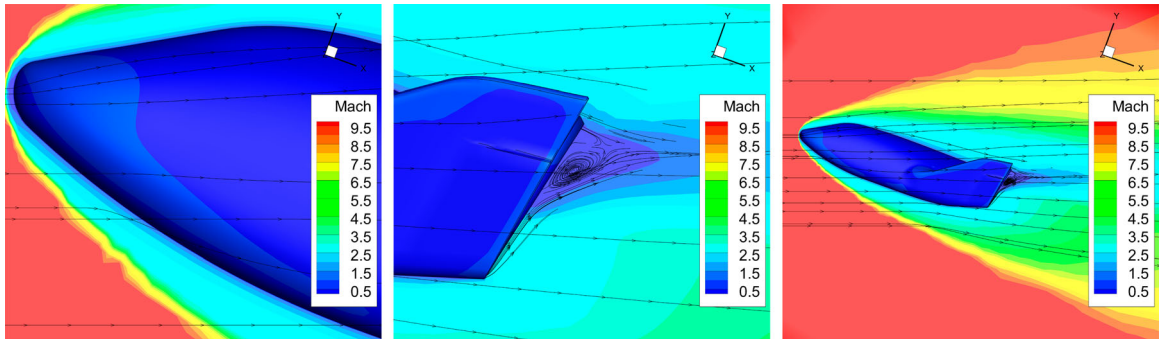


**Figure 26.** Mach distributions and streamlines.

## 5. Discussion and Conclusion

In this paper, in order to increase the accuracy and robustness of the third-order CGKS in three-dimensional flow simulation with unstructured tetrahedral mesh, the scheme is further developed with the modification of multi-resolution WENO reconstruction and the introduction of compression factor (CF) for the updated gradients inside each control volume. Based on the updates of both cell-averaged flow variables and their gradients, in three-dimensional space the direct extension of the WENO reconstruction used in the previous 2D CGKS can easily get failed due to the complicated geometry and deteriorated 3-D unstructured mesh, and leads to the lack of robustness in viscous flow simulations. In order to increase the mesh adaptivity, the multi-resolution WENO scheme is modified to get to the targeted cell only for the reconstruction in extreme cases, which converts the high-order CGKS to the first-order GKS when necessary. On the other hand, due to the use of the continuous assumption of flow variables at the cell interface, the updated gradients of the flow variables through the Divergence theorem around the control volume is problematic in case of the discontinuities. Thus, the CF being proportional to the strength of the discontinuities is introduced to compress the gradients accordingly. Different from identifying the 'trouble cells' and moving them from the high-order discretisation (Krivodonova et al. 2004; Clain, Diot, and Loubère 2011; Xiangxiong Zhang 2017), the current approach is to turn the 'trouble cells' into normal ones through CF and a uniform CGKS is applied everywhere. A detailed illustration about the combination of CF and multi-resolution WENO reconstruction on the improvement of CGKS is given in Appendix. As a result, the current CGKS can use a large explicit time step, improve robustness and mesh adaptability, and have high program portability. The numerical tests, especially in the 3D hypersonic flow computations under complex geometry, demonstrate the validity of the scheme.

## Acknowledgments

The authors would like to thank Mr. Yipei Chen for the help on the setting of the hypersonic space vehicle case.

## Disclosure statement

No potential conflict of interest was reported by the author(s).

## Funding

The current research is supported by National Numerical Windtunnel project and National Science Foundation of China [grant number 11772281], [grant number 91852114].

## References

Antoniadis, Antonis F., Panagiotis Tsoutsanis, and Dimitris Drikakis. 2017. "Assessment of High-Order Finite Volume Methods on Unstructured Meshes for RANS Solutions of Aeronautical Configurations." *Computers & Fluids* 146: 86–104.

Bharti, Ram Prakash, R. P. Chhabra, and V. Eswaran. 2006. "Steady Flow of Power Law Fluids Across a Circular Cylinder." *The Canadian Journal of Chemical Engineering* 84 (4): 406–421.

Bhatnagar, Prabhu Lal, Eugene P. Gross, and Max Krook. 1954. "A Model for Collision Processes in Gases. I. Small Amplitude Processes in Charged and Neutral One-Component Systems." *Physical Review* 94 (3): 511.

Braza, M., P. Chassaing, and H. Ha Minh. 1986. "Numerical Study and Physical Analysis of the Pressure and Velocity Fields in the Near Wake of a Circular Cylinder." *Journal of Fluid Mechanics* 165: 79–130.

Chen, Yipei, Yajun Zhu, and Kun Xu. 2020. "A Three-Dimensional Unified Gas-Kinetic Wave-particle Solver for Flow Computation in All Regimes." *Physics of Fluids* 32 (9): Article ID 096108.

Cheng, Jian, Xiaodong Liu, Tiegang Liu, and Hong Luo. 2017. "A Parallel, High-Order Direct Discontinuous Galerkin Method for the Navier–Stokes Equations on 3D Hybrid Grids." *Communications in Computational Physics* 21 (5): 1231–1257.

Clain, S., S. Diot, and R. Loubère. 2011. "A High-Order Finite Volume Method for Systems of Conservation Law – Multi-Dimensional Optimal Order Detection (MOOD)." *Journal of Computational Physics* 230 (10): 4028–4050.

Coutanceau, Madeleine, and Roger Bouard. 1977. "Experimental Determination of the Main Features of the Viscous Flow in the Wake of a Circular Cylinder in Uniform Translation. Part 1. Steady Flow." *Journal of Fluid Mechanics* 79 (2): 231–256.

Dumbser, Michael. 2010. "Arbitrary High Order PNPM Schemes on Unstructured Meshes for the Compressible Navier–Stokes Equations." *Computers & Fluids* 39 (1): 60–76.

Grove, A. S., F. H. Shair, and E. E. Petersen. 1964. "An Experimental Investigation of the Steady Separated Flow Past a Circular Cylinder." *Journal of Fluid Mechanics* 19 (1): 60–80.

Huynh, Hung T. 2007. A Flux Reconstruction Approach to High-Order Schemes Including Discontinuous Galerkin Methods. In *18th AIAA Computational Fluid Dynamics Conference*, Miami, Florida, 4079.

Ji, Xing. 2019. "High-Order Non-Compact and Compact Gas-Kinetic Schemes." PhD thesis. Hong Kong University of Science and Technology.

Ji, Xing, Fengxiang Zhao, Wei Shyy, and Kun Xu. 2021a. "Compact High-Order Gas-Kinetic Scheme for Three-Dimensional Flow Simulations." *AIAA Journal*, 59 (8): 2979–2996.

Ji, Xing, Fengxiang Zhao, Wei Shyy, and Kun Xu. 2021b. "Two-Step Multi-Resolution Reconstruction-Based Compact Gas-Kinetic Scheme on Tetrahedral Mesh." Preprint, arXiv:2102.01366.

Krivodonova, L., J. Xin, J.-F. Remacle, N. Chevaugeon, and J. E. Flaherty. 2004. "Shock Detection and Limiting with Discontinuous Galerkin Methods for Hyperbolic Conservation Laws." *Applied Numerical Mathematics* 48 (3): 323–338. Workshop on Innovative Time Integrators for PDEs.

Li, Jiequan, and Zhifang Du. 2016. "A Two-Stage Fourth Order Time-Accurate Discretization for Lax–Wendroff Type Flow Solvers I. Hyperbolic Conservation Laws." *SIAM Journal on Scientific Computing* 38 (5): A3046–A3069.

Li, Wanai. 2014. *Efficient Implementation of High-Order Accurate Numerical Methods on Unstructured Grids*. Berlin, Heidelberg: Springer.

Liu, Yangyang, Liming Yang, Chang Shu, and Huangwei Zhang. 2020. "Three-Dimensional High-Order Least Square-Based Finite Difference-Finite Volume Method on Unstructured Grids." *Physics of Fluids* 32 (12): Article ID 123604.

Luo, Hong, Luqing Luo, Robert Nourgaliev, Vincent A. Mousseau, and Nam Dinh. 2010. "A Reconstructed Discontinuous Galerkin Method for the Compressible Navier–Stokes Equations on Arbitrary Grids." *Journal of Computational Physics* 229 (19): 6961–6978.

Nagata, T., T. Nonomura, S. Takahashi, Y. Mizuno, and K. Fukuda. 2016. "Investigation on Subsonic to Supersonic Flow Around a Sphere At Low Reynolds Number of Between 50 and 300 by Direct Numerical Simulation." *Physics of Fluids* 28 (5): Article ID 056101.

Pan, Liang, and Kun Xu. 2016. "A Third-Order Compact Gas-Kinetic Scheme on Unstructured Meshes for Compressible Navier–Stokes Solutions." *Journal of Computational Physics* 318: 327–348.

Pan, Liang, and Kun Xu. 2020. "High-Order Gas-Kinetic Scheme with Three-Dimensional WENO Reconstruction for the Euler and Navier–Stokes Solutions." *Computers & Fluids* 198: Article ID 104401.

Pan, Liang, Kun Xu, Qibing Li, and Jiequan Li. 2016. "An Efficient and Accurate Two-Stage Fourth-Order Gas-Kinetic Scheme for the Euler and Navier–Stokes Equations." *Journal of Computational Physics* 326: 197–221.

Schmitt, V. 1979. *Pressure Distributions on the ONERA M6-Wing at Transonic Mach Numbers, Experimental Data Base for Computer Program Assessment*. AGARD AR-138.

Seal, David C., Yaman Güçlü, and Andrew J. Christlieb. 2014. "High-Order Multiderivative Time Integrators for Hyperbolic Conservation Laws." *Journal of Scientific Computing* 60 (1): 101–140.

Shu, Chi-Wang. 2016. "High Order WENO and DG Methods for Time-Dependent Convection-Dominated PDEs: A Brief Survey of Several Recent Developments." *Journal of Computational Physics* 316: 598–613.

Shu, Chi-Wang, and Stanley Osher. 1989. "Efficient Implementation of Essentially Non-Oscillatory Shock-Capturing Schemes, II." In *Upwind and High-Resolution Schemes*, 328–374. Berlin, Heidelberg: Springer.

Taneda, Sadatoshi. 1956. "Experimental Investigation of the Wakes Behind Cylinders and Plates At Low Reynolds Numbers." *Journal of the Physical Society of Japan* 11 (3): 302–307.

Tang, Tao, and Kun Xu. 1999. "Gas-Kinetic Schemes for the Compressible Euler Equations: Positivity-Preserving Analysis." *Zeitschrift für angewandte Mathematik und Physik ZAMP* 50 (2): 258–281.

Tritton, David J. 1959. "Experiments on the Flow Past a Circular Cylinder At Low Reynolds Numbers." *Journal of Fluid Mechanics* 6 (4): 547–567.

Wang, Qian. June, 2017. "Compact High-Order Finite Volume Method on Unstructured Grids." PhD thesis. Tsinghua University.

Wang, Z. J., Y. Li, F. Jia, G. M. Laskowski, J. Kopriva, U. Paliath, and R. Bhaskaran. 2017. "Towards Industrial Large Eddy Simulation Using the FR/CPR Method." *Computers & Fluids* 156: 579–589.

Xu, Kun. 2001. "A Gas-Kinetic BGK Scheme for the Navier–Stokes Equations and Its Connection with Artificial

Dissipation and Godunov Method." *Journal of Computational Physics* 171 (1): 289–335.
Xu, Kun. 2014. *Direct Modeling for Computational Fluid Dynamics: Construction and Application of Unified Gas-Kinetic Schemes*. Singapore: World Scientific.
Yang, Xiaoquan, Jian Cheng, Hong Luo, and Qijun Zhao. 2019. "Robust Implicit Direct Discontinuous Galerkin Method for Simulating the Compressible Turbulent Flows." *AIAA Journal* 57 (3): 1113–1132.
Yu, Meilin, Z. J. Wang, and Yen Liu. 2014. "On the Accuracy and Efficiency of Discontinuous Galerkin, Spectral Difference and Correction Procedure Via Reconstruction Methods." *Journal of Computational Physics* 259: 70–95.
Zhang, Fan, Jian Cheng, and Tiegang Liu. 2019. "A Direct Discontinuous Galerkin Method for the Incompressible Navier–Stokes Equations on Arbitrary Grids." *Journal of Computational Physics* 380: 269–294.
Zhang, Xiangxiong. 2017. "On Positivity-Preserving High Order Discontinuous Galerkin Schemes for Compressible Navier–Stokes Equations." *Journal of Computational Physics* 328: 301–343.
Zhao, Fengxiang, Xing Ji, Wei Shyy, and Kun Xu. 2020. "A Compact High-Order Gas-Kinetic Scheme on Unstructured Mesh for Acoustic and Shock Wave Computations." Preprint, arXiv:2010.05717.
Zhu, Jun, and Chi-Wang Shu. 2018. "A New Type of Multi-Resolution WENO Schemes with Increasingly Higher Order of Accuracy." *Journal of Computational Physics* 375: 659–683.
Zhu, Jun, and Chi-Wang Shu. 2020. "A New Type of Third-Order Finite Volume Multi-Resolution WENO Schemes on Tetrahedral Meshes." *Journal of Computational Physics* 406: Article ID 109212.

## Appendix

The motivation for modifying cell-averaged slopes on 3D unstructured mesh is to increase the robustness of the scheme, especially on tetrahedral mesh. In 3-D case with a bad mesh topology, the conventional WENO procedure cannot give reliable reconstructions, even though it is usually considered as a robust spatial reconstruction method. As an example, the tetrahedral meshes near the boundary with a small radius of curvature can easily have a high volume ratio and the maximum included angle can become close to 180°. A 2-D example with geometric singularity is shown in Figure A1, where the first-order polynomial $p^1 = Q_0 + a_1(x - x_0) + a_2(y - y_0)$ cannot be properly determined with the centroid $y_0 = y_1 = y_2$. As one of the sub-stencil in the traditional WENO reconstruction, the smoothness indicator from such a sub-stencil cannot be correctly measured by the definition in Equation (16). With two sub-stencils for the targeted cell $\Omega_0$, such that one has bad geometry as shown in Figure A1 in the smooth flow region and the other has good mesh topology in the shock region, the smooth indicators given by these two sub-stencils could be the same and incorrectly evaluated. Then, the WENO reconstruction will give an invalid slope, leading to a reduction in robustness.

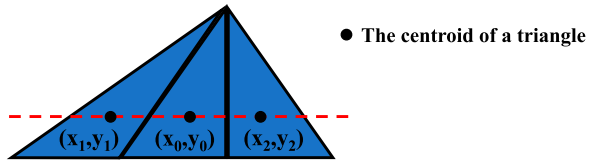


**Figure A1.** A singular 2-D case: the first-order polynomial cannot be constructed by the three cell-averaged values in the stencil.

On the other hand, the first-order finite volume schemes with approximate Riemann solvers are positive-preserving, e.g. the first-order L-F scheme, and the first-order kinetic vector flux-splitting scheme (Tang and Xu 1999). The first-order GKS is also robust enough for the hypersonic flow simulation. In order to recover such a situation, the reconstruction scheme should be able to give one of the sub-stencils with the targeted cell only. Such a new reconstruction strategy can be designed for high-order CGKS to reduce to first-order GKS when necessary. In order to achieve such a goal, the WENO-type reconstruction has to have the following three properties,

(1) The first-order sub-stencil (i.e. the zeroth polynomial $p^0$ determined solely by the cell-averaged conservative variable on the targeted cell) must be included;
(2) The smooth indicator from the above sub-stencil is independent of grid quality;
(3) The smooth indicator from the above sub-stencil should be small enough if a discontinuity is located inside the targeted cell.

The multi-resolution WENO (Zhu and Shu 2018) satisfies Property 1, which has also been adopted in the previous CGKS (Ji et al. 2021b). Since both cell-averaged conservative variables and their slopes are updated in CGKS, a first-order polynomial inside each cell can always be constructed, i.e. $p_i^1 = \overline{W}_i + \overline{W}_{x,i}x_i$. Same as the DG methods (Yang et al. 2019), such type of polynomial has great mesh adaptability. All these polynomials in the compact stencil can be used to evaluate the smooth indicator of $p^0$, which satisfies Property 2, as a 2-D example shown in Figure A2. Property 3 requires the sub-cell resolution of a scheme. In the cases with discontinuities, the updated gradients in CGKS through divergence theorem in Equation (10) may become invalid. This is the reason for the introduction of CF $\alpha$ being proportional to the strength of the discontinuities, as shown in Equation (21), to compress the gradients accordingly. The CF is more of less an indicator of measuring the strength of the sub-cell discontinuity. Both mesh illness and flow continuities have been taken into account through the above WENO reconstruction and CF, as shown in Figure A3, for the 3D CGKS simulation.

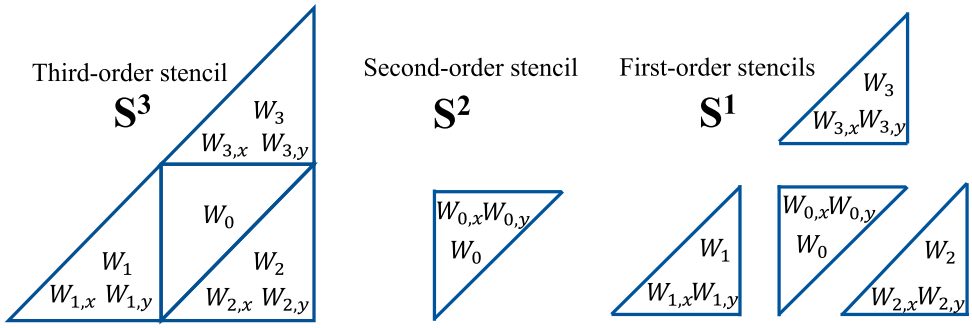


**Figure A2.** A 2-D example for stencil selections for the compact multi-resolution WENO reconstruction.

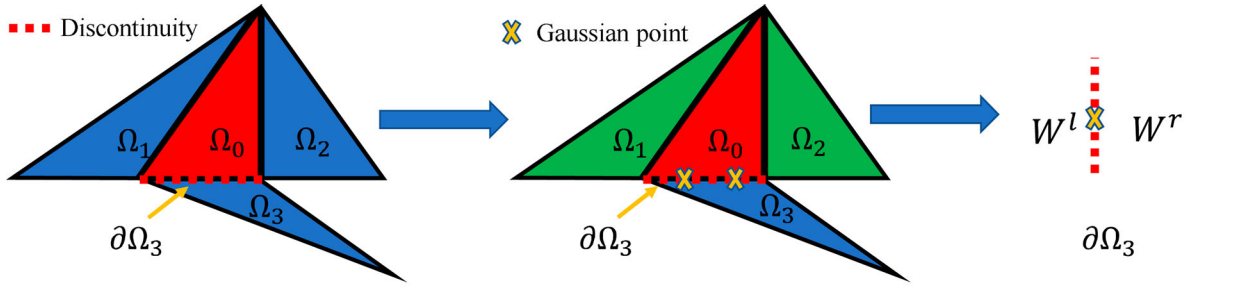


(1) Reconstruction stencil for $\Omega_0$ with bad mesh & discontinuity. There is a discontinuity on interface $\partial\Omega_3$. In traditional WENO, the substencil 1 with $\Omega_0, \Omega_1, \Omega_2$ is singular, while the substencil 2 with $\Omega_0, \Omega_1, \Omega_3$ and substencil 3 with $\Omega_0, \Omega_2, \Omega_3$ cross the discontinuity. All of the substencils fail to correctly measure the local smoothness

(2) New first-order substencils defined in Fig. 28 in $\Omega_1$ and $\Omega_2$ are always non-singular. It leads the WENO reconstruction reduce to first-order accuracy

(3) The discontinuity on $\partial\Omega_3$ is correctly detected and the CF at each Gaussian point on $\partial\Omega_3$ is $\frac{1}{1+|O(1)|}$

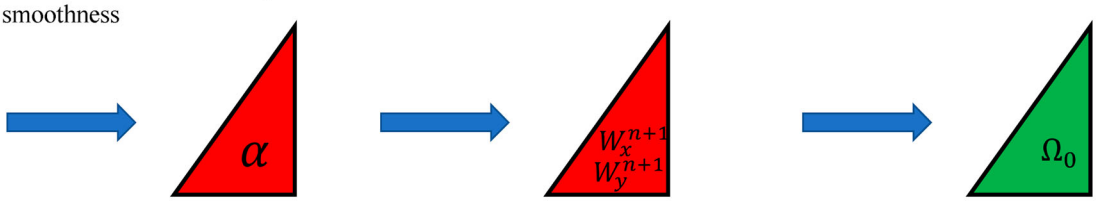


(4) The CF $\alpha \ll 1$ in $\Omega_0$ as defined in Eq. (20), which indicates the subcell discontinuity at $t^{n+1}$

(5) The updated $W_x^{n+1}, W_y^{n+1} \to 0$. The smooth indicator for $\Omega_0$ is $\beta_0 = W_x^2 + W_y^2 \to 0$ and leads the reconstruction involving $\Omega_0$ at $t^{n+1}$ reduce to first-order accuracy

(6) The CGKS with CF reduces to first-order scheme near cells with subcell discontinuity.

**Figure A3.** CF function in case of bad mesh topology and discontinuity.